The Astrophysical Journal, 696:1278–1306, 2009 May 10 doi:10.1088/0004-637X/696/2/1278

THE EXTENDED ENVIRONMENT OF M17: A STAR FORMATION HISTORY

Matthew S. Povich[1], Ed Churchwell[1], John H. Bieging[2], Miju Kang[2,3], Barbara A. Whitney[4], Crystal L. Brogan[5], Craig A. Kulesa[2], Martin Cohen[6], Brian L. Babler[1], Rémy Indebetouw[7], Marilyn R. Meade[1], and Thomas P. Robitaille[8,9]

[1] Department of Astronomy, University of Wisconsin at Madison, 475 N. Charter Street, Madison, WI 53706, USA; povich@astro.wisc.edu
[2] Steward Observatory, University of Arizona, Tucson, AZ 85721, USA
[3] Korea Astronomy and Space Science Institute, Chungnam National University, Daejeon, Korea
[4] University of Colorado, Space Science Institute, 1540 30th Street, Suite 23, Boulder, CO 80303-1012, USA
[5] National Radio Astronomy Observatory, Charlottesville, VA 22903, USA
[6] Radio Astronomy Laboratory, University of California, Berkeley, CA 94720, USA
[7] Department of Astronomy, University of Virginia, P.O. Box 3818, Charlottesville, VA 22903-0818, USA
[8] Harvard-Smithsonian Center for Astrophysics, 60 Garden Street, Cambridge, MA 02138, USA
Received 2008 August 6; accepted 2009 February 21; published 2009 April 23

ABSTRACT

M17 is one of the youngest and most massive nearby star-formation regions in the Galaxy. It features a bright H II region erupting as a blister from the side of a giant molecular cloud (GMC). Combining photometry from the *Spitzer* Galactic Legacy Infrared Mid-Plane Survey Extraordinaire (GLIMPSE) with complementary infrared (IR) surveys, we identify candidate young stellar objects (YSOs) throughout a $1.^{\circ}5 \times 1^{\circ}$ field that includes the M17 complex. The long sightline through the Galaxy behind M17 creates significant contamination in our YSO sample from unassociated sources with similar IR colors. Removing contaminants, we produce a highly reliable catalog of 96 candidate YSOs with a high probability of association with the M17 complex. We fit model spectral energy distributions to these sources and constrain their physical properties. Extrapolating the mass function of 62 intermediate-mass YSOs ($M_{\star} > 3\ M_{\odot}$), we estimate that >1000 stars are in the process of forming in the extended outer regions of M17. The remaining 34 candidate YSOs are found in a 0.17 deg^2 field containing the well-studied M17 H II region and photodissociation region (PDR), where bright diffuse mid-IR emission drastically reduces the sensitivity of the GLIMPSE point-source detections. By inspecting IR survey images from *IRAS* and GLIMPSE, we find that M17 lies on the rim of a large shell structure $\sim 0.^{\circ}5$ in diameter ($\sim$20 pc at 2.1 kpc). We present maps of ^{12}CO and ^{13}CO ($J = 2 \rightarrow 1$) emission observed with the Heinrich Hertz Telescope. The CO emission shows that the shell is a coherent, kinematic structure associated with M17, centered at $v = 19$ km s^{-1}. The shell is an extended bubble outlining the PDR of a faint, diffuse H II region several Myr old. We identify a group of candidate ionizing stars within the bubble. YSOs in our catalog are concentrated around the bubble rim, providing evidence that massive star formation has been triggered by the expansion of the bubble. The formation of the massive cluster ionizing the M17 H II region itself may have been similarly triggered. We conclude that the star formation history in the extended environment of M17 has been punctuated by successive waves of massive star formation propagating through a GMC complex.

Key words: H II regions – infrared: ISM – radio continuum: ISM – radio lines: ISM – stars: formation

1. INTRODUCTION

Most star formation in the local universe is observed to occur in dense, massive clusters of hundreds or thousands of stars that are created by the gravitational collapse and fragmentation of massive cores within giant molecular clouds (GMCs). In the Galaxy, one of the best nearby laboratories for the study of star formation in the environment of a rich, massive cluster is M17, the Omega Nebula. Most of the observational attention given to M17 has focused on the bright "blister" H II region, $\sim 5'$ in diameter, erupting from the side of the M17 molecular cloud, a GMC at a velocity of 20 km s^{-1} with a mass $>3 \times 10^4\ M_{\odot}$ (Lada 1976). The H II region divides the M17 molecular cloud into two components, and following the nomenclature of Wilson et al. (1999) we will refer to the more massive, southern component as "M17 South" and the northern component as "M17 North" (see Figure 1). M17 has served both as an infrared (IR) spectral template for photodissociation regions (PDRs) surrounding bright H II regions (Cesarsky et al. 1996; Verstraete et al. 1996) and as a prototype for H II region structure (Felli et al. 1984; Brogan & Troland 2001; Pellegrini et al. 2007; Povich et al. 2007, hereafter PSC07).

The ionization of the M17 H II region is provided by the rich cluster NGC 6618, which is deeply embedded in the gas and dust of the M17 cloud. Optical and near-IR photometric and spectroscopic studies have uncovered at least 16 O stars and over 100 B stars in NGC 6618 (Ogura & Ishida 1976; Chini et al. 1980; Lada et al. 1991; Hanson et al. (1997); Hoffmeister et al. 2008, hereafter H08). Several water masers have been observed around M17 (Cesarsky et al. 1978), and a prominent hypercompact H II region, M17 UC-1, lies on the interface of the H II region with M17 South (Felli et al. 1984; Sewilo et al. 2004). M17 has been searched repeatedly for massive stars with circumstellar disks (Nielbock et al. 2001; Chini et al. 2004b), and thousands of IR-excess sources have been reported in and around the H II region (Lada et al. 1991; Jiang et al. 2002, hereafter J02; H08) High-resolution observations using the *Chandra X-ray Observatory* have provided a census of the young stellar population of M17 (Broos et al. 2007; hereafter BFT07). BFT07 found IR counterparts for 771 of the 886 X-ray sources in their sample, and they report that only $\sim$10% of these

[9] Spitzer Fellow.

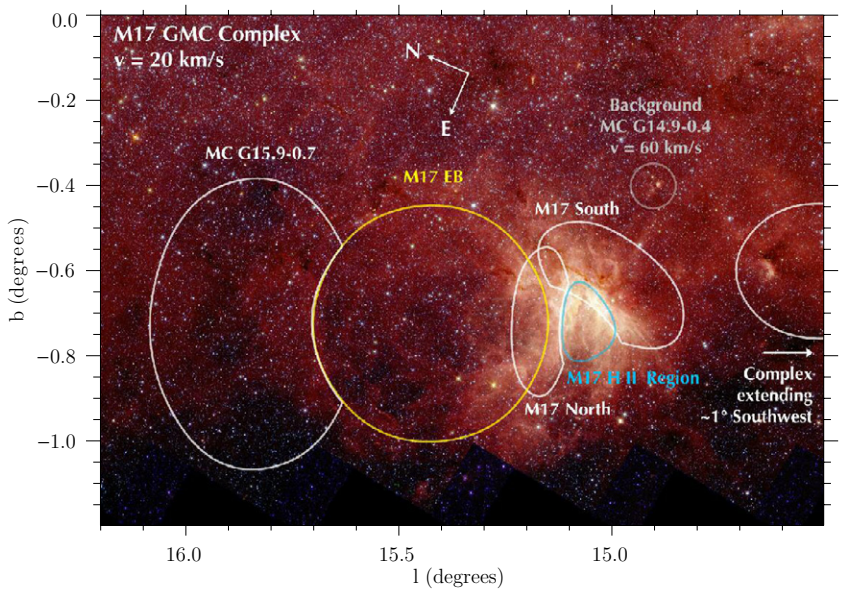

Figure 1. GLIMPSE full-color image of the M17 field (red: 8.0 μm, orange: 5.8 μm, green: 4.5 μm, and blue: 3.6 μm). A schematic diagram showing the approximate boundaries of large-scale structures mentioned in the text is overlaid. The molecular clouds shown in white and gray have been identified from the CO survey data of Sanders et al. (1986).

sources exhibit IR emission in excess of a stellar photosphere due to the presence of dust in circumstellar disks and/or infalling envelopes. Taken together, the observations suggest that, while some fraction of the NGC 6618 stellar population has ceased accreting, massive star formation is ongoing in and around the M17 H II region. Many authors have suggested that the birth of a second generation of massive stars has been triggered on the periphery of the H II region by the expansion of the ionized gas into the M17 molecular cloud (Cesarsky et al. 1978; Felli et al. 1984; Jiang et al. 2002; Hoffmeister et al. 2008).

The extended environment of M17 has often been overlooked. Elmegreen & Lada (1976) presented CO observations of a large molecular cloud complex associated with M17 at $v = 20$ km s^{-1} extending more than 1° to the Southwest, parallel to the Galactic mid-plane (Figure 1). They suggested that the entire complex is undergoing sequential star formation, beginning with the OB stars of NGC 6618 at the northeast tip. Jaffe & Fazio (1982) cast doubt on this sequential star formation scenario by presenting 13 far-IR sources within the extended complex that did not show a progression of decreasing age with increasing distance from M17. Several high-resolution Galactic plane radio surveys in molecular or atomic line emission have included M17 (Sanders et al. 1986; Mizuno & Fukui 2004; McClure-Griffiths et al. 2005). The Massachusetts–Stony Brook Galactic Plane CO Survey (Sanders et al. 1986), which provided (b, v) maps with 45″ resolution that include M17 and its vicinity. The Sanders et al. (1986) CO $J = 1$–0 maps clearly show both the M17 molecular cloud and the complex identified by Elmegreen & Lada (1976), and they reveal an additional molecular cloud at $v = 20$ km s^{-1}, centered at (l, b) = (15.°9, −0.°7). We name this second cloud MC G15.9−0.7 (Figure 1).

Unbiased surveys of the Galactic plane reveal large structures that are missed by pointed observations with limited fields of view. Visual inspection of images from the *Spitzer Space Telescope* Galactic Infrared Mid-Plane Survey Extraordinaire (GLIMPSE) reveals a circular dust shell ∼0.°5 in diameter outlined by faint, diffuse 8 μm emission. M17 marks the Southwest rim of the shell (see Figure 1). This structure is also apparent in *Infrared Astronomy Satellite* (*IRAS*) images at 60 μm and 100 μm. The dust shell appears to extend from M17 to MC G15.9−0.7. Diffuse 8 μm emission is usually attributed to polycyclic aromatic hydrocarbons (PAHs) that fluoresce when illuminated by ultraviolet (UV) radiation. The shell morphology is similar to that of the IR bubbles identified in GLIMPSE by Churchwell et al. (2006). Such bubbles typically outline the PDRs of H II regions (Povich et al. 2007; Watson et al. 2008). The dust shell near M17 was not selected for the GLIMPSE bubbles catalog because it is partially obscured by the bright diffuse emission from M17 and lacks a well-defined inner rim. Nevertheless, we will demonstrate that the shell is an extended bubble outlining the PDR of a large, faint H II region associated with M17. We call this structure the M17 extended bubble (M17 EB; Figure 1).

While the screen of cold, dense molecular gas in M17 South probably prevents the stellar winds and ionizing radiation from the OB stars in NGC 6618 from influencing the extended molecular cloud complex to the Southwest, on the Northeast side of M17 there is evidence that M17 EB is interacting with both MC 15.9−0.7 and M17 itself. The M17 H II region surrounds a central cavity that is filled by hot, diffuse plasma observed by *Chandra* (Townsley et al. 2003; Povich et al. 2007). *ROSAT* observations covering a larger area show soft X-ray emission spilling out of the H II region and apparently filling part of M17 EB; this X-ray emission is spatially coincident with faint Hα emission (Dunne et al. 2003). A search for SIMBAD objects in the interior of M17 EB reveals several stars with OB spectral types. We will show that these stars represent the most massive members of the cluster ionizing M17 EB and that this cluster is both distinct from and older than NGC 6618. We refer to this progenitor cluster as NGC 6618PG.

The distance to M17 has been somewhat disputed in recent years. Most estimates have been based upon optical/near-IR photometry of the most luminous stars. Hanson et al. (1997) reported a distance of $1.3^{+0.4}_{-0.2}$ kpc, a significant departure from the kinematic distance of 2.3 kpc. Nielbock et al. (2001) subsequently employed a revised extinction law (Chini &

Wargau 1998) and derived a distance of 1.6 ± 0.3 kpc. The value of 1.6 kpc has since been widely adopted. PSC07 balanced the flux in the integrated IR spectral energy distribution (SED) of M17 with the bolometric luminosity of all known ionizing stars in NGC 6618 and reported a distance of $1.6^{+0.3}_{-0.2}$ kpc. This luminosity distance assumed both that all of the major ionizing stars in the region were known and, like the previous spectrophotometric distance estimates, that the majority of the known ionizing stars were *not* in unresolved binary or otherwise multiple systems. Recently, Hoffmeister et al. (2008) showed that the most luminous stellar system in M17, the O4+O4 binary star called Kleinmann's Anonymous star or CEN 1 (Chini et al. 1980), is itself composed of two spectroscopic binary systems of nearly equal-mass components. This discovery, along with new distance moduli for other massive stars in NGC 6618, led Hoffmeister et al. (2008) to revise the M17 distance once again, to 2.1 ± 0.2 kpc, in agreement with the kinematic distance. In this work, we will generally adopt the 2.1 kpc distance, but we will also consider 1.6 kpc where the distance uncertainty could significantly impact our results.

We take advantage of the large area surrounding M17 observed by the *Spitzer* Galactic plane surveys to investigate star formation in the extended environment of M17, emphasizing the newly discovered structures to the Northeast. We have combined GLIMPSE with longer-wavelength IR survey data from both the Multiband Imaging Photometer for *Spitzer* (MIPS) Galactic plane survey (MIPSGAL) and the *Midcourse Space Experiment* (MSE). We use these datasets to investigate the population of young stellar objects (YSOs), identified by their IR excess emission, over a large ($\sim 1.5^\circ \times 1^\circ$) area surrounding M17. Our investigation includes the full spatial extent of the M17 molecular cloud, M17 EB, and MC G15.9−0.7. We have followed up the IR survey data with high-resolution ^{12}CO and ^{13}CO $J = 2$–1 observations. In Section 2 we summarize our observations and data reduction. We describe our methods for selecting and characterizing YSO candidates in Section 3, and we discuss the extended young stellar population of M17 in relation to the molecular cloud structures in Section 4. In Section 5, we synthesize these results into a picture of propagating massive star formation in M17, and we summarize our conclusions in Section 6.

2. OBSERVATIONS AND DATA PROCESSING

2.1. IR Galactic Plane Survey Data

2.1.1. GLIMPSE

As part of the *Spitzer* Legacy Science Program, GLIMPSE (Benjamin et al. 2003) imaged the Galactic plane from $|l| = 0^\circ$–65°, $|b| \leqslant 1^\circ$ using the four mid-IR bands (3.6, 4.5, 5.8, and 8.0 μm) of the Infrared Array Camera (IRAC) on the *Spitzer Space Telescope* (Fazio et al. 2004). High-resolution (1.″2 pixels) image mosaics were created by the GLIMPSE pipeline[10] from Basic Calibrated Data (BCD) image frames processed by the *Spitzer* Science Center (SSC). The GLIMPSE point-source extractor, a modified version of Daophot (Stetson 1987) was used to extract point sources from the individual image frames. The 5σ point-source detection limits of the GLIMPSE are nominally 0.2, 0.2, 0.4, and 0.4 mJy for the [3.6], [4.5], [5.8], and [8.0] bands, respectively, and higher in regions of bright diffuse emission. Flux densities of sources detected at greater than 5σ at least twice in one or more of the four IRAC bands were included in the GLIMPSE Point Source Archive. The highly reliable GLIMPSE Point Source Catalog is a subset of the Archive. Both the Archive and the Catalog incorporated JHK_S flux densities from the Two Micron All Sky Survey (2MASS) point source catalog (Skrutskie et al. 2006) to produce final sourcelists containing flux densities from 1–8 μm in seven near- to mid-IR bands. For this study, we use the GLIMPSE v2.0 Point Source Archive and the GLIMPSE v3.0 image mosaics. The majority of the Archive sources used in our analysis will also appear in the highly reliable Catalog because of our additional requirement that each source must be detected in at least four bands (see Section 3.2). We use the Archive instead of the catalog because the Archive identifies sources with near-saturated fluxes that can later be used as lower limits and contains more sources in crowded regions. Mosaics produced from 2MASS data provide near-IR images that complement GLIMPSE.

2.1.2. MIPSGAL

We downloaded 24 μm and 70 μm post-BCD mosaics of the MIPSGAL survey (Carey et al. 2009) from SSC. The 24 μm mosaics have 2.″4 pixels and the 70 μm mosaics have 4.″8 pixels. MIPSGAL point-source catalogs were not yet available at the time of this study, so we extracted 24 μm point-source fluxes using the GLIMPSE extractor. Because the GLIMPSE pipeline software is not optimized for MIPSGAL data, this procedure generates the following types of false source detections: noise peaks, small resolved structures, and artifacts from the point-spread function wings of bright sources. As a first cut to reduce the number of false sources in our analysis, we removed all 24 μm sources with larger than 25% error in measured flux density ($F/\delta F < 4$) from the sourcelist. We then spatially correlated (bandmerged) the 24 μm sources with the GLIMPSE Archive sources. If an Archive source was located within 2.″4 of the central position of a 24 μm source, the source was considered to have a 24 μm detection and the [24] flux was appended to the Archive fluxes. If more than one Archive source was located within 2.″4 of a 24 μm source, the [24] flux was appended as an upper limit for each correlated Archive source. The correlation procedure favors "true" 24 μm point sources because these are more likely to have a GLIMPSE counterpart, but occasionally a false source or false correlation makes it into the bandmerged list. The final eight-band (combined 2MASS, GLIMPSE, and MIPSGAL [24]) sourcelists were inspected by eye to reject any remaining suspicious sources (see Section 3.2).

2.1.3. Aperture Photometry

We did not attempt to automatically extract MIPSGAL [70] point source fluxes. Only ∼10 obvious 70 μm unresolved sources are visible in the BCD mosaics within our analysis region, so we extracted the [70] fluxes of interesting sources manually, using aperture photometry. Visual inspection of the GLIMPSE mosaics revealed ∼10 compact red sources that are resolved by IRAC and hence not in the Archive. Such sources may be luminous YSOs that heat ambient dust in molecular clouds out to a few pc distance. One pc corresponds to 78 1.″2 GLIMPSE mosaic pixels at 2.1 kpc. Our aperture photometry procedure used the Funtools[11] package with the SAOImage DS9[12] image display program to extract fluxes from

[10] Details of the data processing can be found at http://www.astro.wisc.edu/glimpse/docs.html.

[11] See http://hea-www.harvard.edu/RD/funtools/ds9.html.

[12] See http://hea-www.harvard.edu/RD/ds9/ref.

apertures defined by eye. For each source extracted, we used the same target apertures for the seven 2MASS+IRAC bands and increased the aperture size as needed for the two MIPSGAL bands. We varied the position of the background sampling a minimum of three times to estimate the contribution of the background subtraction to the flux uncertainty. Although the background subtraction generally dominated the uncertainty on the extracted fluxes, our uncertainty estimates also included photon counting statistics (prior to the correction for Zodiacal emission) and the uncertainty introduced by applying the IRAC extended aperture corrections[13] to sources with effective radii $> 9''$.

2.1.4. MSX

The Spirit III instrument on board the MSX satellite surveyed the Galactic plane in four IR bands (Price et al. 2001): *A* (isophotal wavelength 8.28 μm), *C* (12.13 μm), *D* (14.65 μm), and *E* (21.3 μm). The 5σ point-source detection limits for MSX are 100, 1100, 900, and 200 mJy for *A*, *C*, *D*, and *E* bands, respectively. The sensitivity of the MSX *A* and *E* bands is just below the saturation limits of IRAC and MIPS, so these bands can be used to replace the fluxes of point sources saturated at IRAC [8.0] and MIPS [24], respectively. The spatial resolution of the MSX images is $\sim 18\farcs3$, so confusion is an issue when correlating MSX Catalog[14] sources with the GLIMPSE Archive. After selecting YSO candidates based on the combined GLIMPSE and MIPS [24] photometry (see Section 3.1), we correlated only the brightest saturated and near-saturated YSO candidates with the MSX catalog, using a $6''$ correlation radius. We did not use the *IRAS* Point-Source Catalog for this work because its low resolution causes too much confusion with multiple GLIMPSE sources.

2.2. CO Observations with the Heinrich Hertz Submillimeter Telescope

We mapped the M17 region in the $J = 2 \rightarrow 1$ transitions of ^{12}CO and ^{13}CO with the 10 m Heinrich Hertz Telescope (HHT) on Mt. Graham, Arizona between 2008 February and 2008 June. The receiver was a dual polarization superconductor-insulator-superconductor (SIS) mixer system employing single-sideband (SSB) mixers with outputs for both upper and lower sidebands, each with a 4–6 GHz IF band. The ^{12}CO $J = 2 \rightarrow 1$ line at 230.538 GHz was placed in the upper sideband and the ^{13}CO $J = 2 \rightarrow 1$ line at 220.399 GHz in the lower sideband, with a small offset in frequency to ensure that the two lines were adequately separated in the IF band, since the sideband rejection was typically 17–20 dB. The spectrometers, one for each of the two polarizations and the two sidebands, were filter banks with 256 channels of 1 MHz width and separation. At the observing frequencies, the spectral resolution was 1.3 km s^{-1} and the angular resolution of the telescope was $32''$ (FWHM). A set of $10' \times 10'$ fields were mapped with on-the-fly (OTF) scanning in R.A. at $10''$ per sec with row spacing of $10''$ in declination, over a total of 60 rows. Each field required about 2 hr of elapsed time. System temperatures were calibrated by the standard ambient temperature load method (Kutner & Ulich 1981) after every other row of the map grid. Atmospheric conditions were generally clear and stable, and the system temperatures were usually nearly constant at $T_{\rm sys} \sim 200$ K (SSB) for each $10' \times 10'$ field.

Data for each polarization and CO isotopomer were processed with the *CLASS* reduction package (from the University of Grenoble Astrophysics Group), by removing a linear baseline and convolving the data to a square grid with $10''$ grid spacing (equal to approximately one-third the telescope beamwidth). The intensity scales for the two polarizations were determined from observations of W51D (W51-IRS2) made just before the OTF maps. The gridded spectral data cubes were processed with the *Miriad* software package (Sault et al. 1995) for further analysis. The two polarizations were averaged for each sideband, yielding images with rms noise per pixel and per velocity channel of 0.15 K-T$^*_A$ for both the ^{12}CO and ^{13}CO transitions.

We mapped a total of 26 $10' \times 10'$ fields, arranged in a semi-regular pattern to cover the main M17 H II region and M17 EB. These 26 fields were combined onto a common spatial grid and converted to Galactic coordinates for comparison with the GLIMPSE images.

3. YSO SELECTION AND CHARACTERIZATION

An overview of the target field of the GLIMPSE survey searched for YSOs is presented in Figure 1, with the approximate boundaries of the M17 H II region, the bubble M17 EB, and the major molecular cloud structures from Sanders et al. (1986) overlaid. The top of the image is the Galactic mid-plane ($b = 0^\circ$), and the jagged bottom edge is the boundary of the GLIMPSE survey between $b = -1^\circ$ and -1.2°. Most of this image is occupied by the molecular cloud complex at $v = 20$ km s^{-1} that includes M17. A smaller cloud, MC G14.9-0.4 associated with compact, bright diffuse mid-IR emission, lies in the background at $v = 60$ km s^{-1}.

We identify candidate YSOs in this image based on their IR excess emission, with the goal of determining the YSO population associated with M17. The location of M17 near the Galactic mid-plane and only 15° from the Galactic center produces a long sightline through the Galaxy in the mid-IR that passes through multiple spiral arms; hence we expect that the GLIMPSE Archive contains many YSOs or other objects with similar IR colors that lie at different distances, unassociated with M17. The average extinction produced by the molecular clouds in the target field is too low to significantly reduce the number of background sources detected in the mid-IR (see Section 4.1.1). Because M17 is bounded in longitude by potentially star-forming molecular clouds and in latitude by the Galactic mid-plane and the survey edge, there is no portion of the GLIMPSE image in Figure 1 that could be used as an off-source region to estimate the contamination in our sample from foreground or background sources (see Section 3.3). Fortunately, the region symmetric to M17, reflected above the Galactic mid-plane, lacks obvious CO emission marking molecular clouds (Sanders et al. 1986; Mizuno & Fukui 2004) and is correspondingly free of the bright diffuse 8.0 μm emission in GLIMPSE that usually identifies H II regions. We selected a circular control field of $0\fdg5$ radius centered at $(l, b) = (15\fdg08, 0\fdg61)$. Since this region has the same Galactic longitude and absolute latitude occupied by M17 but exhibits no obvious signs of massive star formation, it can be used to address the question of what the Galactic plane would look like if M17 were not present. We analyzed the control field in parallel with the M17 target field, using the same procedure to select candidate YSOs from both fields.

[13] See http://ssc.spitzer.caltech.edu/irac/calib/extcal/.
[14] See http://irsa.ipac.caltech.edu/applications/Gator/.

Table 1
Source Counts in the YSO Search

Sources	M17 Target Field (1.67 deg^2)		Control Field (0.78 deg^2)	
	Number	Density (deg^{-2})	Number	Density (deg^{-2})
In GLIMPSE Archive	352,225	211,000	191,010	245,000
Fit with SED Models ($N_{\rm data} \geqslant 4$)	126,385	75,700	71,391	91,500
Well Fit by Stellar Photosphere SEDs ($\chi^2/N_{\rm data} \leqslant 5$)	124,768	74,700	70,628	90,500
Poorly Fit by Stellar Photosphere SEDs ($\chi^2/N_{\rm data} > 5$)	1617	970	763	980
Well Fit by YSO SEDs ($\chi^2/N_{\rm data} \leqslant 5$)	979	590	370	470
In Final Sample of YSO Candidates	406	240	106	140
In M17 YSO Candidate Subsample[a]/Control Subsample[b]	195	205	25	100

Notes.
[a] Irregularly shaped region with area 0.95 deg^2 (See Section 4).
[b] Square box centered at $(l, b) = (15.^\circ1, 0.^\circ7)$ with area 0.25 deg^2.

3.1. Fitting YSO Model Spectral Energy Distributions to Broadband IR Fluxes

Our principal tools for identifying and characterizing candidate YSOs from this rich dataset were the grid of YSO models from Robitaille et al. (2006, hereafter RW06) and the SED fitting tool of Robitaille et al. (2007, hereafter RW07). The model grid consists of 20,000 two-dimensional Monte Carlo radiation transfer models (Whitney et al. 2003a, 2003b, 2004) spanning a complete range of stellar mass and evolutionary stage and output at 10 viewing angles (inclinations), so the model fitting tool actually has 200,000 SEDs to choose from. The model fitting tool uses a fast χ^2-minimization linear regression algorithm (RW07). We can robustly distinguish between YSOs and reddened photospheres of main-sequence and giant stars because YSOs require a thermal emission component from circumstellar dust to reproduce the shapes of their mid-IR excesses. The Monte Carlo radiative transfer models upon which the fitting tool relies have been tested extensively by successfully fitting the SEDs of numerous well-characterized YSOs in Taurus (RW07). The models and fitting tool have also been employed to analyze the YSO populations of the Eagle Nebula (Indebetouw et al. 2007), several other Galactic massive star formation regions observed as part of GLIMPSE (Shepherd et al. 2007; Watson et al. 2008), and the Large Magellanic Cloud (Whitney et al. 2008).

The radiation transfer technique employed in the RW06 models propagates "photons" from the central source through the circumstellar environment. The models solve for the temperature structure of the circumstellar material and include absorption and re-emission by dust along with photons produced by disk accretion and backwarming of the stellar photosphere (Whitney et al. 2003a, 2003b, 2004). When we fit models to observed YSOs, we essentially use Monte Carlo radiation transfer to look through the veil of circumstellar dust, placing the central star on the H-R diagram by interpolating between pre-main-sequence (PMS) evolutionary tracks (Bernasconi & Maeder 1996; Siess et al. 2000).

Like all complex models, the YSO models have built-in assumptions, degeneracies, and a multidimensional parameter space to explore. In general, fitting these models to real data results in many different sets of parameters that can describe a YSO almost equally well. Rather than attempt (futilely) to find a unique solution, we accept a range of well-fit models to investigate how well we can *constrain* the physical properties of each YSO. The distance to the modeled sources places an important external constraint on the allowable luminosities of the well-fit YSO models. For M17, we used the distance range of 1.6–2.3 kpc, effectively building the distance uncertainty into our constraints on the YSO properties from the model parameters. The number of acceptable models also decreases rapidly with increasing range of IR wavelengths from available data included in the SED.

The steps of our process for selecting candidate YSOs are outlined in Table 1, along with the number and density of sources in both the target and control fields at each step. We began by removing sources with SEDs that are consistent with stellar photospheres. We fit all sources that are detected in $N_{\rm data} \geqslant 4$ of the eight near- through mid-IR bands in the GLIMPSE Archive combined with MIPSGAL 24 μm fluxes (126,385/352,225 sources in the target field and 71,391/191,010 sources in the control field; Table 1) with SEDs from 7853 model stellar atmospheres (Brott & Hauschildt 2005) included in the RW07 fitting tool. Interstellar extinction based upon the mid-IR extinction law of Indebetouw et al. (2005) was included in the model fits, so even highly reddened stars (we allow a maximum A_V of 30 mag when fitting stellar photosphere SEDs) returned good fits. We considered all sources with a best-fit χ^2, normalized by the number of flux data points used in the fit, satisfying $\chi^2/N_{\rm data} \leqslant 5$ to be well-fit by stellar photospheres. We determined this threshold value by visual inspection of the best-fit SEDs for a variety of sources. To avoid biasing the fits for sources where the flux uncertainties have been underestimated, before fitting any models we conservatively reset the uncertainties to a floor value of $\delta F/F = 10\%$ for all sources in the GLIMPSE Archive with $\delta F/F < 10\%$. For the MIPS [24] fluxes, we used an uncertainty floor of 15%.

We then took the 1617 sources in the target field and 763 sources in the control field that were poorly fit by stellar photospheres and fit them a second time using the RW06 YSO models. Again, we considered sources with a best-fit $\chi^2/N_{\rm data} \leqslant 5$ to be well fit, and these formed the basis of our YSO sample. The vast majority of sources that were well-fit neither by stellar photospheres nor YSO models are actually stars with saturated fluxes or poor photometry (often in the [24] band where our photometry is less robust) or signs of variability (a mismatch between 2MASS and GLIMPSE photometry due to the different epochs of the observations). Eleven sources in the target field appeared to be good YSO candidates with marginal fits. Several of these had saturated fluxes in one or more bands, and one (G015.6653−00.4989) exhibited excess emission in the [4.5] band similar to previously studied sources associated with molecular outflows (Smith et al. 2006; Davis et al. 2007; Shepherd et al. 2007; Cyganowski et al. 2008). These

were moved to the "well-fit" sample after the questionable flux measurements were replaced with upper or lower limits.

3.2. A Highly Reliable Sample of Candidate YSOs

Our primary goal was to produce a highly reliable sample of candidates YSO. As shown in Table 1, only 979/126,385 or 0.77% of sources fit with SED models in the M17 target field were fit well by YSO models but could not be fit well by stellar photospheres. This fraction was significantly lower for the control field, with 370/71,391 or 0.5% of sources (the counting uncertainty is 0.02%). While the model fitting process performed the service of discarding the >99% of sources that we were not interested in studying, simply being well fit by YSO model SEDs was a necessary but insufficient criterion for a source to be included in the final sample. As a last step, we culled sources from the sample by inspecting all of the SED fits by eye, in many cases returning to the GLIMPSE and MIPSGAL images to confirm visually the existence of a valid source in each band with a reported detection. Two common reasons to reject a well-fit YSO candidate necessitated this final inspection:

1. The IR excess emission that prevented the source from being fit well by stellar photosphere models occurs only in the IRAC [8.0] band, with no detection at MIPS [24]. Such an SED can be produced by poor source extraction in regions with highly structured diffuse emission or a Malmquist bias affecting faint sources in the GLIMPSE sourcelists. The Malmquist bias occurs because when a source is selected for the Archive on the basis of a 5σ detection in any combination of bands, the fluxes of the remaining bands can be entered in the Archive even if they are at lower confidence levels. Stars are typically faint at 8 μm, and often a noise peak or a diffuse background feature can be extracted from the position of a star observed in the other bands, causing an artificially high measured [8.0] flux. While a few of the sources exhibiting this SED may actually be YSOs, we make the conservative decision to discard all questionable candidates.
2. A suspicious IR excess is observed in the MIPS [24] band only. The difference in resolution between MIPS and IRAC increases the chance of a false match when correlating sources between MIPSGAL and GLIMPSE. This often happens near bright, saturated 24 μm sources where the extended wings of the MIPS point-spread function can be extracted as individual point sources and matched with an overlapping GLIMPSE source. This creates a spurious 24 μm excess attributed to the GLIMPSE source.

Both of the above issues constitute important caveats to consider if searching for YSOs possessing "transition disks" with large inner holes that might have been cleared out by planets, since such sources exhibit IR excess emission only at longer wavelengths.

The brightest sources in our sample also appear in the MSX point source catalog, so we used available MSX fluxes to fill in the SED between IRAC and MIPS and replace saturated IRAC [8.0] and MIPS [24] fluxes, where possible. Bright sources with very red SEDs from K–[8.0] that are isolated from other IR-excess sources are candidate evolved stars on the asymptotic giant branch (AGB). Carbon stars, for example, have mean absolute K-band magnitudes of ~6.8 (Wallerstein & Knapp 1998) and are often enshrouded by dusty envelopes generated by strong winds (Guandalini et al. 2006); such stars have similar SEDs to YSOs from K to [8.0] and, even when located on the far side of the Galaxy, will be among the brightest sources observed in GLIMPSE. The RW07 fitting tool incorporates 75 AGB star SED templates derived from *Infrared Space Observatory* (*ISO*) spectroscopy (Sylvester et al. 1999; Hony et al. 2002). After fitting bright sources with the AGB star templates, we removed 30 and 15 likely AGB stars from the target and control samples, respectively.

Example SEDs of two probable AGB stars and two bright candidate YSOs from the target field are plotted in Figure 2. The most distinctive features of the AGB star SEDs are the precipitously red K–[8.0] spectral index and the turnover to a Rayleigh–Jeans spectrum at wavelengths longward of ~24 μm. The YSO models that fit the SEDs of these bright sources tend to be massive stars with optically thick disks but without substantial infalling envelopes. Such objects are relatively rare, the best example in M17 being the Kleinmann–Wright (KW) Object (Kleinmann & Wright 1973), a suspected Herbig Be star (Chini et al. 2004a). The SED of the KW Object is plotted in the upper right panel of Figure 2. Several candidate YSOs, including the one shown in the lower right panel of Figure 2, are detected at 70 μm by MIPSGAL, but no candidate AGB stars are observed at 70 μm. Generally, YSO disks and envelopes contain cool ($T_d \sim 30$ K) dust that becomes optically thin at relatively large radii from the central star, while the dust distribution in AGB stellar winds has a much smaller effective radius, giving higher effective temperatures ($T_d \gtrsim 200$ K). It is therefore reasonable to expect that the SEDs of AGB stars will peak at shorter wavelengths than those of YSOs, but this difference cannot be observed without data at wavelengths of 24 μm or longer, and there may be exceptions to this general rule.

Visual inspection of the M17 target field revealed six bright, compact resolved IRAC sources that have SEDs well-fit by YSO models. These sources are noted in Tables 2–4 (see Section 4.1.2). Four of the six are MSX point sources, and their SEDs are suggestive of a PAH spectrum. The model fits to these sources were improved dramatically by assuming PAHs contributed significantly to the emission in the four bands with the strongest PAH features, IRAC [5.8] & [8.0] and MSX A & C. The RW06 YSO models did not include emission from PAHs; hence to fit sources with potentially PAH-dominated spectra we set these four bands as upper limits. Using the fluxes of the well-fit models to estimate the continuum levels in the bands affected by PAHs, we find that PAHs contribute anywhere from 30% to 90% of the broadband fluxes. The YSO models for three of these four sources indicate central stars with photospheric temperatures of $T_{\rm eff} \sim 2 \times 10^4$ K, hot enough to produce the UV radiation necessary to excite PAH transitions (Povich et al. 2007, and references therein). The fourth source, F53 in Table 3, was fit by few high-$T_{\rm eff}$ models. This object appears to be associated with the molecular cloud MC G14.9-0.4 (see Figure 1), giving it a near kinematic distance of 4.8 kpc at the cloud velocity of 60 km s^{-1}. This is far beyond the maximum distance of 2.3 kpc given to the model fitting tool, and at the larger distance this source is likely to be a compact H II region. This interpretation is supported by the fact that the source also appears to have associated radio emission from the 11 cm continuum survey of Reich et al. (1990). For consistency, we leave this source in the final sample of candidate YSOs, but we exclude it, along with other sources listed in Table 3 that are found outside the M17 subregion defined in Section 4.1, from the analysis of YSOs associated with M17.

Table 2
Candidate YSOs in the Extended Environment of M17

Index No.	l (deg)	b (deg)	[4.5] (mag)	[8.0] (mag)	[24] (mag)	$M_\star$ ($M_\odot$) Min	$M_\star$ ($M_\odot$) Max	$\log(L_{TOT}/L_\odot)$ Min	$\log(L_{TOT}/L_\odot)$ Max	Evolutionary Stage[a]
The Bridge										
E1	14.7207	−0.4859	6.4	6.0	3.3	6	6	3.1	3.2	II
E2	14.7392	−0.4736	12.0	10.4	5.7	0.3	4	0.1	2.2	Amb.
E3	14.7762	−0.4657	7.4	6.8	3.9	6	6	3.1	3.2	II
E4	14.7776	−0.4900	9.7	9.5	5.8	1	4	1.3	2.1	Amb.
E5	14.7963	−0.4565	12.3	11.2	6.9	1	4	1.3	2.5	II
E6	14.8039	−0.5135	7.4	7.0	4.3	3	6	2.1	2.9	II
E7	14.8214	−0.5136	7.5	6.5	2.8	4	8	2.4	3.4	II
E8	14.8217	−0.4782	11.3	11.1	6.8	0.6	4	0.6	1.7	0/I
E9	14.8291	−0.5279	9.2	8.4	4.8	3	5	1.8	2.6	II
E10	14.8462	−0.4890	12.7	11.9	7.0	0.2	4	0.1	1.7	Amb.
The Outer Regions of the M17 GMC										
E11	14.8338	−0.6974	9.6	8.8	6.0	3	5	1.7	2.6	II
E12	14.9743	−0.5079	11.7	9.8	> 3.3	0.3	4	0.4	2.3	Amb.
E13	15.1289	−0.4958	11.5	9.0	3.2	0.2	5	1.0	2.7	0/I
E14	15.1426	−0.4883	11.4	9.8	> 4.1	0.2	5	0.5	2.8	II
E15	15.1473	−0.5299	9.2	8.3	3.5	1	5	1.5	2.5	Amb.
E16	15.1511	−0.4837	10.2	9.2	5.8	2	4	1.3	2.3	II
E17	15.1971	−0.6266	7.0	5.7	...	5	10	2.6	3.5	Amb.
E18	15.2039	−0.6325	8.2	7.3	...	3	6	2.1	2.7	II
E19	15.2052	−0.6451	9.2	...	...	3	9	2.1	3.7	Amb.
E20	15.2336	−0.6279	9.2	7.8	3.2	0.2	5	0.9	2.5	Amb.
M17 EB										
E21	15.3512	−0.3525	10.7	10.1	6.8	2	4	1.0	2.0	II
E22	15.3555	−0.2921	9.8	8.7	2.5	0.9	6	1.3	2.4	0/I
E23	15.3572	−0.3770	10.3	9.4	4.7	0.9	4	1.0	2.4	Amb.
E24	15.3599	−0.2973	11.4	10.5	5.2	0.2	4	0.2	2.1	0/I
E25[b]	15.3649	−0.4164	7.2	3.4	< −0.4	6	10	2.9	3.4	Amb.
E26	15.3708	−0.3350	7.1	6.4	2.4	5	6	2.6	3.0	II
E27	15.3733	−0.3714	12.9	12.5	7.7	0.2	3	-0.2	1.6	Amb.
E28	15.3886	−0.3073	10.9	10.1	5.9	0.8	4	0.8	2.0	Amb.
E29	15.3990	−0.3633	12.9	10.7	7.1	1	5	0.5	2.7	Amb.
E30	15.4620	−0.7198	10.3	9.5	6.2	2	4	1.3	2.2	II
E31	15.4854	−0.7175	4.6	3.7	1.7	9	10	3.6	3.7	II
E32	15.4878	−0.4327	12.8	11.8	6.9	0.1	4	-0.1	1.8	Amb.
E33	15.4932	−0.4162	11.7	10.1	5.9	0.4	4	0.6	2.4	II
E34	15.5115	−0.9519	9.9	8.8	6.7	2	7	1.3	3.3	II
E35	15.5202	−0.4190	10.9	10.0	> 5.4	0.7	4	0.8	1.7	II
E36	15.5221	−0.4880	8.2	7.0	2.4	0.2	1	1.3	1.6	0/I
E37	15.5268	−0.4078	11.1	11.3	> 6.1	0.9	1	1.0	1.1	0/I
E38	15.5281	−0.4207	12.5	11.9	> 4.6	0.2	4	0.3	1.7	0/I
E39	15.5326	−0.3903	12.5	11.2	8.0	0.4	4	0.1	2.2	II
E40	15.5330	−0.4066	10.6	9.4	> 5.3	3	6	1.8	2.9	II
E41	15.5437	−0.9338	9.0	7.3	4.0	3	8	2.1	3.4	Amb.
E42	15.5471	−0.3938	11.9	11.5	7.5	0.3	4	0.1	1.7	II
E43	15.5489	−1.0066	8.3	> 5.6	< 0.2	2	7	2.2	2.7	0/I
E44	15.5502	−1.0063	10.1	8.0	> 0.2	1	5	1.4	2.0	0/I
E45	15.5553	−0.4603	7.1	6.2	2.5	5	8	2.9	3.4	II
E46	15.5583	−0.4646	12.6	11.0	> 1.1	0.2	5	0.4	2.2	0/I
E47	15.5584	−0.4622	6.5	< 5.0	1.1	5	10	2.8	3.8	II
E48	15.5625	−0.3870	13.3	11.0	4.9	0.1	5	0.4	2.0	0/I
E49	15.5691	−0.5076	12.0	11.2	7.4	0.9	3	0.4	1.4	II
E50	15.6050	−0.4788	11.4	10.4	6.7	0.6	4	0.5	2.1	II
E51	15.6092	−0.4878	12.0	10.5	5.4	0.1	4	0.0	2.3	Amb.
E52	15.6385	−0.5225	10.1	9.0	6.0	2	3	1.2	1.7	II
E53	15.6448	−0.4847	13.0	...	6.1	0.1	4	-0.0	2.4	Amb.
E54	15.6588	−0.5279	10.2	9.4	5.8	3	4	1.7	2.5	II
E55[c]	15.6653	−0.4989	9.2	9.5	0.7	7	8	2.6	3.0	0/I
E56	15.6918	−0.8014	11.2	10.7	8.3	2	3	0.8	1.5	III
E57	15.7296	−0.7243	13.5	11.4	7.0	0.2	4	0.0	2.0	II
E58	15.7408	−0.6349	12.0	11.2	8.1	0.5	3	0.3	1.7	II
E59	15.7478	−0.6914	13.1	10.7	5.5	0.1	4	0.2	2.1	Amb.
E60	15.7677	−0.7310	10.6	9.4	5.4	1	4	1.1	2.4	II

Table 2
(Continued)

Index No.	l (deg)	b (deg)	[4.5] (mag)	[8.0] (mag)	[24] (mag)	$M_\star$ ($M_\odot$) Min	$M_\star$ ($M_\odot$) Max	$\log(L_{TOT}/L_\odot)$ Min	$\log(L_{TOT}/L_\odot)$ Max	Evolutionary Stage[a]
MC G15.9−0.7 (Likely Unassociated)										
E61	15.8856	−0.6053	9.0	8.7	6.0	3	4	1.7	2.2	II
E62	15.9210	−0.6134	12.6	11.9	8.4	0.3	3	-0.1	1.6	II

Notes. The sources presented in this table are found within the white boundary lines but outside the rectangle in Figure 10. While the association of any given source with M17 is uncertain, the groupings of candidate YSOs are significant. The "Bridge" is a molecular gas structure connecting the M17 molecular cloud with the GMC complex extending 85 pc to the southwest. Although our cluster-finding algorithm selects 2 candidate YSOs apparently located in MC 15.9−0.7, these sources are likely unassociated.
[a] "Amb." means that the well-fit models are divided between different evolutionary stages
[b] Source E25 is resolved by IRAC and is also an *MSX* point source. Its SED exhibits PAH emission.
[c] Source E55 is the candidate protostar shown in Figure 12.

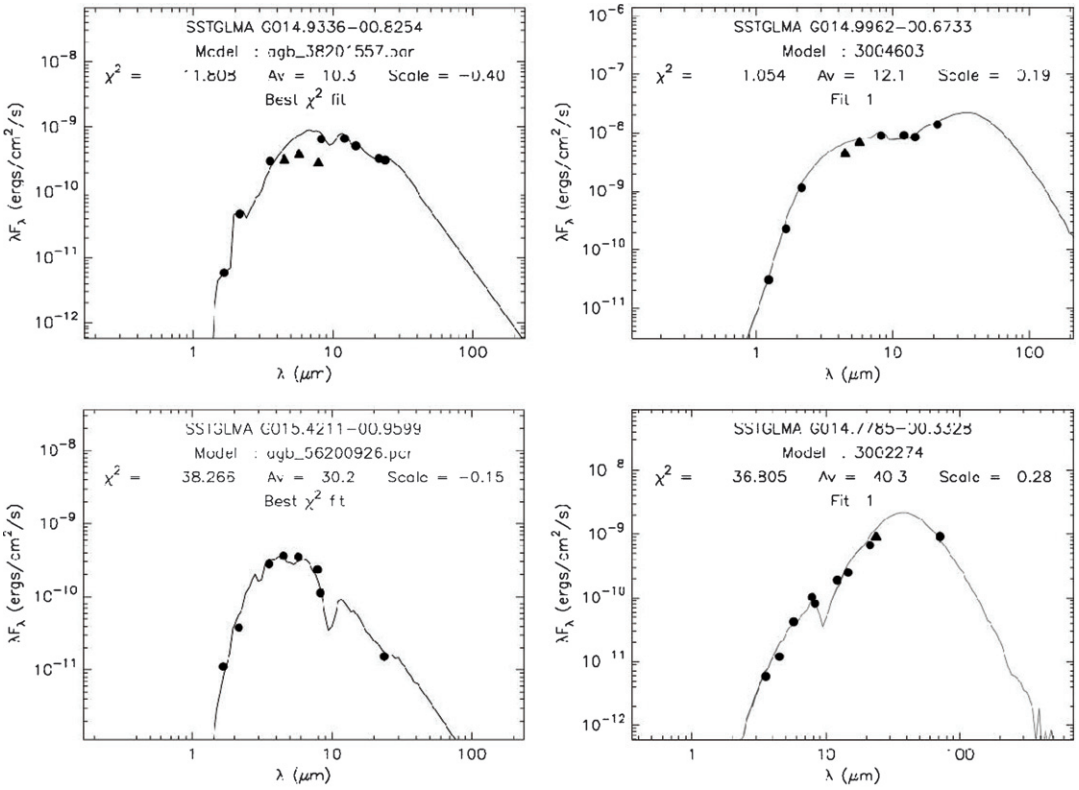

Figure 2. Example plots of best-fit model SEDs to available near- and mid-IR photometry. Two sources well fit by AGB star spectral templates (left panels) are compared to two sources well fit by YSO models (right panels) with similar brightnesses. Triangles denote data points with saturated fluxes that were used only as lower limits for the model fitting. The best-fit SED to the KW Object is plotted in the upper right panel.

3.3. YSO Evolutionary Stages

RW06 divided the YSO models into evolutionary stages according to the envelope accretion rate $\dot{M}_{\rm env}$ and the circumstellar disk mass $M_{\rm disk}$, both normalized by the mass of the central star $M_\star$:

$$\text{Stage 0/I}: \quad \dot{M}_{\rm env}/M_\star > 10^{-6}\,{\rm yr}^{-1}$$
$$\text{Stage II}: \quad \dot{M}_{\rm env}/M_\star < 10^{-6}\,{\rm yr}^{-1}; \quad M_{\rm disk}/M_\star > 10^{-6}$$
$$\text{Stage III}: \quad \dot{M}_{\rm env}/M_\star < 10^{-6}\,{\rm yr}^{-1}; \quad M_{\rm disk}/M_\star < 10^{-6}.$$

These YSO classifications are based upon model parameters corresponding to physical properties, but they parallel the popular observational T Tauri classification system that uses IR spectral indices (Lada 1987). Stage 0/I YSOs are protostars heavily embedded in the infalling gas and dust of their natal envelopes. Stage II YSOs, like Class II T Tauri stars, have optically thick circumstellar disks that dominate their near- to mid-IR SEDs. Stage III YSOs have optically thin remnant disks and their SEDs are dominated by photospheric emission; these objects are difficult to identify by IR excess alone (given our error bars of $\geqslant$ 10%–15%), hence very few examples are found in our conservative YSO sample. Because each candidate YSO was fit with multiple YSO models, we determined the evolutionary stage of each source statistically. We defined the set of "well-fit" models to each source as those models with fits meeting the criterion of

$$\frac{\chi^2}{N_{\rm data}} - \frac{\chi^2_{\rm min}}{N_{\rm data}} \leqslant 2, \qquad (1)$$

where $\chi^2_{\rm min}$ is the goodness-of-fit parameter for the best-fit model. We estimated the *relative* probability of each model

Table 3
Other Candidate Clustered YSOs in the M17 Target Field

Index No.	l (deg)	b (deg)	[4.5] (mag)	[8.0] (mag)	[24] (mag)	Group[a]
F1	14.5865	−0.5708	10.6	9.1	4.9	SW
F2	14.5898	−0.5822	12.8	11.6	7.3	SW
F3	14.5999	−0.5422	10.2	9.7	6.3	SW
F4	14.6005	−0.6248	9.9	9.9	5.6	SW
F5	14.6017	−0.6177	10.9	10.1	5.3	SW
F6	14.6043	−0.6229	10.3	9.7	6.4	SW
F7	14.6116	−0.5520	11.2	9.9	5.7	SW
F8	14.6117	−0.6259	9.7	9.3	6.4	SW
F9	14.6148	−0.5843	11.4	10.4	> 5.7	SW
F10	14.6235	−0.5775	10.7	9.9	> 5.5	SW
F11	14.6285	−0.5781	9.5	8.6	> 4.6	SW
F12	14.6290	−0.7614	12.5	···	5.3	SW
F13	14.6297	−0.5724	11.1	10.1	> 5.4	SW
F14	14.6311	−0.5784	10.6	9.3	> 2.1	SW
F15	14.6314	−0.5774	11.7	10.2	2.1	SW
F16	14.6327	−0.5719	10.9	10.2	> 6.4	SW
F17	14.6348	−0.8730	13.1	12.1	8.1	SW
F18	14.6395	−0.7286	11.6	11.3	8.3	SW
F19	14.6416	−0.8928	13.1	11.8	6.1	SW
F20	14.6426	−0.7639	11.2	9.7	5.3	SW
F21	14.6428	−0.8833	12.3	11.5	7.2	SW
F22	14.6437	−0.9011	10.9	10.3	6.8	SW
F23	14.6533	−0.7411	12.6	11.5	8.2	SW
F24	14.6660	−0.8838	12.6	11.9	8.0	SW
F25	14.6745	−0.8863	10.9	10.6	7.0	SW
F26	14.6771	−0.7672	9.7	9.0	5.1	SW
F27	14.6802	−0.8755	11.8	10.6	6.0	SW
F28	14.6990	−0.8916	12.3	11.9	6.9	SW
F29	14.7720	−0.3570	···	8.6	3.1	
F30	14.7868	−0.2176	11.9	10.2	> 6.4	
F31	14.7878	−0.2353	10.9	10.5	7.3	
F32	14.7952	−0.2062	12.0	11.7	7.7	
F33	14.7999	−0.2072	12.6	11.1	7.7	
F34	14.8122	−0.2346	9.9	9.3	6.4	
F35	14.8209	−1.0206	8.0	7.4	4.7	SW
F36	14.8247	−0.2663	11.7	10.2	5.9	
F37	14.8302	−0.1774	11.1	10.7	2.2	
F38	14.8443	−1.0049	6.9	6.4	3.3	SW
F39	14.8516	−0.9890	> 10.7	10.1	3.2	SW
F40	14.8519	−0.9927	> 10.8	10.0	3.2	SW
F41	14.8521	−1.0007	11.4	10.7	7.7	SW
F42	14.8522	−0.3314	11.5	11.0	7.8	
F43	14.8566	−0.1674	13.0	12.1	> 7.0	
F44	14.8607	−0.4358	10.1	9.4	6.8	MC G14.9
F45	14.8621	−0.1594	13.8	12.1	7.6	
F46	14.8624	−0.9974	12.8	11.8	8.0	SW
F47	14.8637	−0.1750	11.0	10.7	7.0	
F48	14.8695	−0.3952	11.3	9.9	5.9	MC G14.9
F49	14.8709	−0.3886	11.9	···	5.5	MC G14.9
F50	14.8747	−0.4154	10.8	9.2	5.7	MC G14.9
F51	14.8840	−0.3558	12.4	···	7.0	
F52	14.8844	−0.3114	11.7	···	6.3	
F53[b]	14.8891	−0.4018	6.1	2.5	< −1.0	MC G14.9
F54	14.8892	−0.1977	11.8	11.1	7.4	
F55	14.8951	−0.4004	11.2	7.6	> 2.9	MC G14.9
F56	14.8993	−0.2249	10.0	9.7	5.2	
F57	14.9224	−0.2113	12.9	12.0	8.1	
F58	14.9234	−0.2147	12.3	···	5.4	
F59	14.9251	−0.4058	9.2	8.9	5.8	MC G14.9
F60	14.9261	−0.1578	12.4	···	7.9	
F61	14.9314	−0.2239	12.4	···	8.0	
F62	14.9340	−0.1358	11.1	10.3	7.0	
F63	14.9346	−0.2295	12.0	11.7	7.7	
F64	14.9372	−0.4296	10.5	9.8	6.2	MC G14.9
F65	14.9378	−0.4229	11.8	···	7.9	MC G14.9
F66	14.9402	−0.1474	11.7	11.1	7.8	
F67	14.9607	−0.1868	6.8	6.1	3.3	
F68	14.9622	−0.1400	9.7	9.4	6.6	
F69	14.9685	−0.1384	11.6	10.8	7.8	
F70	14.9764	−0.2147	12.0	10.5	6.3	
F71	14.9804	−0.4319	10.0	9.2	6.2	
F72	14.9960	−0.3090	11.2	10.8	7.8	
F73	15.0626	−0.2450	10.7	10.2	7.2	
F74	15.0634	−0.3109	10.8	10.2	7.4	
F75	15.0768	−0.2528	11.4	10.7	6.7	
F76	15.0773	−0.2511	11.1	10.2	7.1	
F77	15.0784	−0.2678	12.4	11.6	7.1	
F78	15.0795	−0.2609	9.2	8.3	4.2	
F79	15.0817	−0.2699	13.0	11.7	> 5.2	
F80	15.0832	−0.2686	10.1	9.2	5.2	
F81	15.0841	−0.1548	10.8	10.0	6.5	
F82	15.1135	−0.1485	9.6	7.8	4.7	
F83	15.1512	−0.1216	11.9	11.2	6.5	
F84	15.1530	−0.1909	12.4	9.7	4.9	
F85	15.1684	−0.1267	11.2	11.4	4.1	
F86[b]	15.1761	−0.1585	12.0	9.4	3.7	
F87[b]	15.1831	−0.1625	7.8	4.7	< −0.5	
F88	15.1841	−0.1589	8.9	6.6	> 1.2	
F89[b]	15.1850	−0.1561	9.7	6.1	> 2.3	
F90	15.1898	−0.1400	12.2	11.6	7.1	
F91	15.1904	−0.1692	12.6	9.9	> 5.9	
F92	15.2199	−0.1451	10.8	9.7	> 4.1	
F93	15.2354	−0.1750	9.1	8.3	5.7	
F94	15.5750	−0.3101	11.0	10.4	> 6.5	Bu G15.7
F95	15.5754	−0.3218	12.3	11.1	7.2	Bu G15.7
F96	15.5815	−0.2963	11.1	9.9	> 6.3	Bu G15.7
F97	15.5869	−0.3003	9.1	8.3	3.7	Bu G15.7
F98	15.5920	−0.2923	13.4	10.9	6.6	Bu G15.7
F99	15.5998	−0.2861	10.8	10.3	6.6	Bu G15.7
F100	15.6028	−0.2040	9.5	8.6	5.0	Bu G15.7
F101	15.6051	−0.2537	11.3	10.6	6.6	Bu G15.7
F102	15.6337	−0.2282	10.3	9.7	> 6.0	Bu G15.7
F103	15.6408	−0.2189	7.9	> 6.2	1.0	Bu G15.7
F104	15.6541	−0.2249	11.6	7.9	2.1	Bu G15.7
F105	15.6603	−0.1189	11.4	9.1	5.6	
F106	15.6638	−0.1231	9.9	9.1	5.7	
F107	15.6747	−0.1476	10.5	···	5.4	
F108	15.6768	−0.1465	11.9	8.2	4.6	
F109	15.6781	−0.2651	10.3	9.9	6.2	Bu G15.7
F110	15.6807	−0.2613	10.7	8.9	5.2	Bu G15.7
F111	15.6829	−0.1424	10.3	9.3	5.6	
F112	15.6929	−0.2576	11.4	11.1	7.6	Bu G15.7
F113	15.6929	−0.1355	10.5	7.0	2.2	
F114	15.6956	−0.1367	10.8	10.5	> 2.2	
F115	15.7181	−0.1648	10.6	9.3	> 3.0	
F116	15.7237	−0.2617	11.5	10.5	7.3	Bu G15.7
F117	15.7250	−0.2480	11.9	11.5	5.0	Bu G15.7
F118	15.7574	−0.2234	12.2	8.8	4.7	
F119	15.7580	−0.1887	8.9	8.2	5.8	
F120	15.7600	−0.2195	9.3	8.6	6.1	
F121	15.7826	−0.3897	12.1	10.5	6.5	
F122	15.7848	−0.3864	12.8	···	7.4	
F123	15.7911	−0.2355	11.3	10.3	6.0	
F124	15.7951	−0.4058	> 11.8	12.1	7.0	
F125	15.7991	−0.3927	9.9	8.8	5.5	
F126	15.8012	−0.3760	8.8	8.4	5.6	
F127	15.8067	−0.3818	12.0	11.2	7.5	
F128	15.8108	−0.2328	11.7	10.5	8.0	

Table 3
(Continued)

Index No.	l (deg)	b (deg)	[4.5] (mag)	[8.0] (mag)	[24] (mag)	Group[a]
F129	15.8113	−0.2394	12.6	11.1	6.8	
F130	15.8367	−0.2653	10.9	9.9	6.3	
F131	15.8612	−0.2350	11.1	···	5.7	
F132	15.9580	−0.1866	11.8	10.7	6.3	
F133	15.9750	−0.2097	9.5	8.3	3.9	
F134	15.9920	−0.2097	12.1	10.6	4.6	
F135	15.9930	−0.1868	10.9	10.7	6.4	

Notes. The sources presented in this table are found outside the white boundary lines in Figure 10. The majority of these sources are at unknown distances.

[a] Groups of these candidate YSOs are apparently associated with prominent molecular cloud structures: "SW" refers to the near end of the large GMC complex at $v = 20$ km s^{-1} extending southwest from M17; "MC G14.9" refers to the molecular cloud G14.9-0.4 at $v = 60$ km s^{-1} (see Figure 1); and "Bu G15.7" refers to an IR/CO shell structure, 4′ in diameter, centered at $(l, b) = (15.^{\circ}67, -0.^{\circ}29)$ and $v \approx 45$ km s^{-1}.

[b] These four sources are resolved by IRAC. F53, F87, and F89 are detected by *MSX* and may be compact H II regions ionized by young clusters rather than single YSOs.

in the set according to

$$P(\chi^2) = e^{-(\chi^2 - \chi^2_{\rm min})/2} \quad (2)$$

and normalized such that $\Sigma P = 1$. This allowed us to construct a probability distribution for the evolutionary stage of each source from the stages of all the well-fit models. The most probable stage of each source was defined by $\Sigma P(\text{Stage}) \geqslant 0.67$; if this condition could not be met, then the stage of the source was considered to be ambiguous.

The 406 candidate YSOs in the final sample of the M17 target field are overplotted as circles on a GLIMPSE [8.0] image in Figure 3. The color-coding of the circles corresponds to the most probable evolutionary stage of each source. Candidate YSOs are distributed throughout the image (the absence of sources from the top and right margins of the image is due simply to the boundaries of our search area). Numerous small "clusters" of 5–10 YSOs are apparent, and larger groups are associated with the M17 molecular cloud and the rim of M17 EB. Candidate YSOs associated with the M17 molecular cloud would dominate the sample if not for the strong masking effect of the bright diffuse mid-IR emission from the H II region and PDR. The point-source detection limit rises dramatically near the M17 H II region, and only the most luminous YSOs are detectable within the area where the 8.0 μm image in Figure 3 appears black. The MIPSGAL 24 μm image is completely saturated within the H II region, and a relatively high fraction of candidate YSOs near the H II region have ambiguous stage (*magenta* circles) because 24 μm fluxes are an important discriminator between disk- and envelope-dominated sources (RW06).

3.4. Mid-IR Color–Color Plots

In Figures 4 and 5 we compare our model-based classifications of all stars and YSOs in the M17 target field with classification systems derived from IRAC mid-IR colors (Allen et al. 2004, hereafter A04; Gutermuth et al. 2008, hereafter G08). A04 showed, through a study of several nearby young clusters, that a box-shaped region in the IRAC [3.6] − [4.5] versus [5.8] − [8.0] color–color diagram (shown in Figures 4) contains primarily Class II YSOs with disks. A04 found that protostars were located in the redward extension of this "disk domain" along both color axes. G08 built upon the work of A04 to devise a more sophisticated system for the classification of YSOs in the young embedded cluster NGC 1333, utilizing multiple IRAC color–color planes. In Figures 4 and 5 the YSO selection and classification criteria of A04 and G08 are compared to our YSO selection and stage classification using the RW06 models. Sources plotted in Figures 4(a), (b) and 5(a),(b) are color-coded according to their most probable evolutionary stage from the RW06 models: red, orange, green, and *lavender* for Stages 0/I, II, III, and ambiguous, respectively, while gray dots represent sources best fit by stellar photospheres, and blue dots show sources that were well fit by YSO models but were excluded from the final sample (see Section 3.2 above). Figures 4(b) and 5(b) show only sources for which the classification using model fitting differs from the classification using the G08 color–color criteria (sources with ambiguous stage are not plotted). In Figures 4(c) and 5(c), sources are plotted according to their G08 color classification: protostars are red while Class II sources are orange. Like virtually all classification systems based upon colors, neither the A04 nor the G08 criteria allow ambiguity between protostars and Class II sources, but we stress that *ambiguity is an inherent property of any YSO taxonomy, whether based upon colors, spectral indices, or SEDs.*

Although the A04 disk domain contains many disk sources, it does not contain *all* candidate disk sources and selects a significant number of diskless stars with reddened photospheres. The locus of Stage II sources in Figure 4(a) is redder than the disk domain by [3.6]−[4.5] ∼ 0.3 mag. The same displacement was found by Indebetouw et al. (2007) for YSOs in the Eagle Nebula (M16), another massive star formation region near the Galactic mid-plane, located ∼2.°5 from M17. The discrepancy could be largely resolved by reddening the disk domain by an amount equivalent to $A_V \approx 20$ mag, a reasonable modification considering that the regions studied by A04 were not highly reddened massive star formation regions in the Galactic plane. The G08 color classification selects 1882 Class II sources and 57 protostars that we find to be well fit by reddened stellar photospheres (gray dots in Figures 4(b) and 5(b)). These sources are a striking feature of Figure 4(c), where they are found predominantly to the left of the disk domain, in the locus of photospheres (A08). Largely on account of these sources, the total number of YSOs selected by the A04 criteria or especially the G08 criteria is far greater than the number of candidate YSOs in our conservative sample. Again, the fact that the G08 color criteria were derived through the study of a nearby star formation region located away from the Galactic plane would explain the large number of reddened stellar photospheres selected as YSOs. In addition, both the A04 and G08 criteria were derived from studies of regions that, unlike M17 and M16, lack many massive YSOs, which should contribute to the disparities between the color–color classifications and the model-based classifications (Whitney et al. 2004).

When compared to our evolutionary stage classifications, the G08 classification system confuses a significant number of protostars for more evolved YSOs, and vice versa. This disagreement is evident in Figure 4, but it can be more readily explained by examination of Figure 5, in which sources are plotted using a color–color diagram that combines IRAC with MIPS [24] photometry. As shown by RW06, this color space illustrates the value of 24 μm data for distinguishing between protostars (Stage 0/I) and disk-dominated (Stage II) YSOs. Figure 5(a) shows a progression toward less evolved sources

Table 4
Candidate YSOs in the Region Observed By *Chandra*

Index No.	l (deg)	b (deg)	[4.5] (mag)	[8.0] (mag)	$M_\star$ ($M_\odot$) Min	$M_\star$ ($M_\odot$) Max	log($L_{TOT}/L_\odot$) Min	log($L_{TOT}/L_\odot$) Max	Evolutionary Stage[a]
With X-ray Counterparts									
X1	14.9846	−0.6718	9.9	8.7	2	3	1.2	1.6	II
X2[b]	14.9855	0.6716	10.6	9.6	1	5	1.0	2.5	II
X3	14.9954	−0.6332	8.4	5.7	1	7	2.1	2.8	0/I
X4[c]	14.9962	−0.6733	< 3.6	···	9	10	3.7	3.9	II
X5	14.9994	−0.6304	7.3	6.9	5	6	2.6	3.2	II
X6	15.0198	−0.6768	8.6	···	4	10	2.3	3.8	II
X7[b]	15.0386	−0.6513	6.2	···	6	15	3.0	4.4	Amb.
X8	15.0470	−0.7023	9.9	8.3	1	5	1.1	2.7	Amb.
X9	15.0530	−0.6934	7.1	6.0	5	9	2.6	3.6	Amb.
X10	15.0568	−0.6068	9.9	8.1	2	5	1.5	2.0	0/I
X11	15.0699	−0.6646	9.4	6.8	1	5	1.3	2.4	0/I
X12	15.1146	−0.6079	11.4	···	1	7	1.1	2.6	0/I
X13	15.1613	−0.6335	10.4	9.5	0.5	4	0.8	1.9	Amb.
X14[b]	15.1772	−0.6593	9.0	8.2	2	5	1.5	2.3	II
Without X-ray Counterparts									
NX1[d]	14.8923	−0.6556	11.0	10.1	2	4	1.1	2.0	II
NX2[d]	14.9277	−0.6740	8.0	7.5	4	5	2.3	2.7	II
NX3[d]	14.9278	−0.6473	11.5	10.3	0.4	7	0.7	2.7	0/I
NX4	14.9761	−0.7292	11.3	···	0.4	7	0.8	3.0	0/I
NX5[e]	14.9791	−0.6651	6.6	3.3	8	11	3.5	3.9	Amb.
NX6	14.9806	−0.6787	11.0	9.9	0.5	5	1.0	2.4	Amb.
NX7	15.0494	−0.6838	7.6	···	4	10	2.2	3.8	Amb.
NX8	15.0576	−0.6830	10.8	8.7	0.6	7	1.0	2.9	0/I
NX9	15.0589	−0.5735	10.8	9.9	0.5	4	0.7	1.5	Amb.
NX10[f]	15.0848	−0.6631	7.7	6.5	2	10	2.1	3.6	Amb.
NX11	15.0895	−0.5641	11.0	9.2	0.7	5	1.0	2.6	0/I
NX12	15.0984	−0.6658	6.3	6.0	5	14	2.9	4.2	III
NX13	15.1176	−0.5618	9.2	8.3	3	7	2.0	2.7	0/I
NX14[d]	15.1337	−0.8681	10.3	8.5	0.4	6	1.0	3.0	II
NX15[d]	15.1348	−0.8683	13.0	10.7	0.2	6	0.3	2.3	0/I
NX16	15.1366	−0.6657	···	5.8	7	14	3.2	4.2	0/I
NX17	15.1784	−0.6299	10.5	9.6	0.3	3	0.7	1.6	Amb.
NX18	15.1808	−0.6222	8.2	6.7	0.5	8	1.5	2.9	0/I
NX19[d]	15.1844	−0.8984	···	5.6	5	8	2.9	3.3	II
NX20	15.2017	−0.8404	8.5	7.5	2	9	2.0	3.2	0/I

Notes.
[a] The "Amb." stage designation is the same as in Table 2.
[b] Selected as X-ray emitting candidate "protostars" in Table 7 of BFT07.
[c] X4 is the KW Object (see Figure 13).
[d] These six sources are located away from the bright 8 μm emission of the M17 PDR, increasing the odds that they are unassociated contaminants.
[e] NX5 is resolved by IRAC (see Figure 13).
[f] NX10 is located at the tip a prominent pillar structure in the M17 H II region. Jiang et al. (2002) resolve this source into two YSOs of comparable brightness in the near-IR, a Class I and a Class II/III candidate. The Class I source likely dominates the mid-IR emission.

with increasing [8.0] − [24] color, and many sources with ambiguous stage determinations (*lavender*) lie along the boundary between the Stage 0/I and II populations. In Figure 5(b), all Stage II sources (orange dots) plotted for [3.6] − [5.8] > 1.5 are protostars according to the G08 classification system (these sources are red dots in Figure 5(c)), which relies upon photometry at wavelengths $\leqslant$8.0 μm.

Two main classes of "false" YSOs are illustrated in the IRAC color–color plots of Figures 4. (1) Candidate AGB stars (open blue circles) are intermingled with YSOs and appear very difficult if not impossible to distinguish by IRAC colors alone. (2) The lower right part of Figure 4(a), centered on [3.6]−[4.5] = 0 for 1 < [5.8]−[8.0] < 2.5, contains numerous sources well fit by YSO models (blue dots) that were discarded from the final sample because the IR excess emission appears at [8.0] only (see Section 3.1 above).

Spurious correlations of 24 μm sources with IRAC sources can also create artificial IR excesses (see Section 3.1), and consequently many sources discarded from our final YSO sample appear in Figure 5(a) as blue dots near [3.6] − [5.8] = 0 for 2 < [8.0] − [24] < 4. Candidate AGB stars are better distinguished from YSOs in Figures 5 than in Figures 4. Three candidate AGB stars (see Section 3.2 above) with [3.6]−[5.8] $\geqslant$ 1.5 but [8.0] − [24] < 1 are located far from YSOs and stellar photospheres. Several other candidate AGB stars have [8.0] − [24] ∼ 2, placing them on the blue edge of the Stage II YSO locus. This supports the interpretation that AGB stars are typically surrounded by dust shells with smaller effective radii

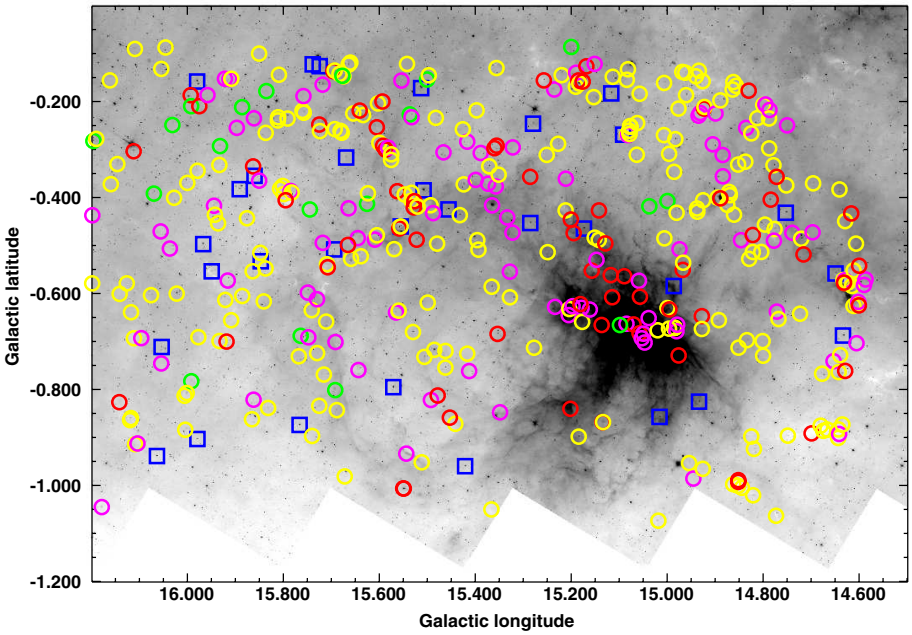

Figure 3. GLIMPSE 8.0 μm image of the M17 analysis target field (inverted logarithmic gray scale). Positions of the 406 candidate YSOs in the final sample are marked by circles color-coded according to the most probable evolutionary Stage of each source: red circles are Stage 0/I candidates (deeply embedded in infalling envelopes); yellow are Stage II (optically thick circumstellar disks); green are Stage III (optically thin circumstellar disks); and *magenta* are candidate YSOs for which the stage is more ambiguous. Blue squares denote candidate AGB stars removed from the YSO sample. The apparent lack of candidate YSOs in the extreme top and right portions of the image reflects the boundaries of the search area.

than the disks and envelopes of YSOs (see Robitaille et al. 2008, for example).

We have experimented with the A04 and G08 color–color criteria for selecting and classifying candidate YSOs because these are among the most well-developed analysis techniques available for IRAC. It is not appropriate to apply these precise color cuts directly to the interpretation of sources in the M17 region, because they were developed through the study of relatively nearby ($d < 1$ kpc) regions that, unlike M17, are located in relatively low-density molecular clouds away from the Galactic plane. This illustrates one of the principal advantages of the model-fitting approach. *All methods for selecting populations of objects based on broadband photometric colors are based upon models.* The RW07 model fitter, with its integrated capacity to apply interstellar extinction to SED models before matching them with observed fluxes, can be employed consistently for the study of star formation in various environments without the need to empirically redraw the selection criteria. A second major advantage is the ability to use all available photometric information simultaneously to constrain the physical parameters of large numbers of sources. For more on the advantages of the model-fitting approach, see Indebetouw et al. (2007).

3.5. Contaminants in the YSO Sample

Even the most carefully selected sample of candidate YSOs will identify other objects that have similar IR colors. External, dusty galaxies are the most common contaminant in YSO searches using deep IRAC observations of nearby star formation regions away from the Galactic plane, such as the c2d Survey (Porras et al. 2007). The GLIMPSE is a shallow survey, and employing the Porras et al. (2007) criterion for galaxy selection to our final M17 target sample of YSOs yields no galaxy candidates (the control sample contains a single source that may be a galaxy). In the Galactic plane, the objects most likely to masquerade as YSOs in significant numbers are evolved stars, specifically AGB stars with dusty winds and unresolved planetary nebulae (PNe). In addition, because we are primarily interested in analyzing the population of YSOs associated with M17, YSOs in the foreground or background must also be treated as contaminants to our sample.

A GLIMPSE 8.0 μm image of the control field is presented in Figure 6, with the final sample of 106 candidate YSOs and AGB stars overplotted as in Figure 3. Candidate YSOs are distributed throughout the search area with an average density of 140 sources deg^{-2}, or nearly 60% of the average source density in the target sample (see Table 1). The source density in the control sample is not uniform, decreasing with increasing Galactic latitude across the 1-degree span of the field, which implies a low Galactic scaleheight for the source population. Because of this variation, we define a box $0.^{\circ}5$ on a side centered at $(l, b) = (15.1, 0.7)$ in the control field, to sample directly the density of contaminants at Galactic latitudes mirroring the location of M17. The source density in this control subfield is 100 deg^{-2} (Table 1).

The control sample represents the contamination expected to be present in the sample of candidate YSOs in the M17 target field. To estimate the numbers of evolved stars expected in the control and target samples, we turned to a detailed model of the IR point source sky (Wainscoat et al. 1992; Cohen 1993). This Sky model incorporates 87 different source populations, including PNe and several types of AGB stars, into a geometric representation of the Galactic bulge, halo, and thin and thick disks. The model has been shown to agree well with *IRAS* observations (Wainscoat et al. 1992).

Cumulative source densities as functions of [4.5] magnitude are presented in Figure 7. Curves generated by the Sky model for oxygen-rich AGB stars (AGB M), optically visible/obscured carbon stars (AGB C/CI), and PNe are plotted along with YSO candidates detected in the target and control samples and subsamples (see Section 4). One striking feature of these plots is the high brightness of AGB stars in the IR. The

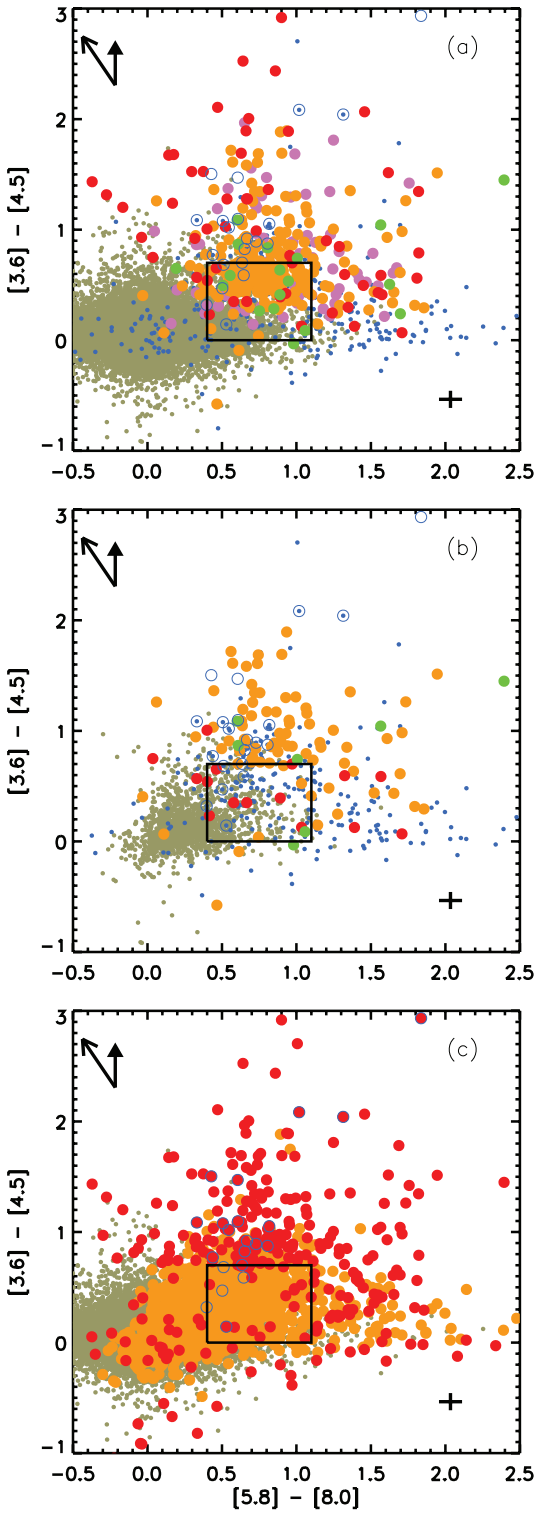

Figure 4. Mid-IR color–color space showing sources in the target field that were detected in all 4 IRAC bands. The "disk domain" of A04 is contained within the black box. (*a*) Candidate YSO selection and classification from model fitting. Small gray dots are sources well fit by stellar photosphere SEDs. Large dots are sources in the final YSO sample (red: Stage 0/I; orange: Stage II; green: Stage III; and *lavender:* ambiguous). (*b*) Sources for which our model-based classification differs from the IRAC color–color classification of G08. Sources discarded from the final YSO sample (small blue dots) remain in this plot if they have IRAC colors consistent with YSOs according to G08. (*c*) G08 YSO selection and classification (gray: stellar photospheres; red: protostars; and orange: Class II). In all plots, blue circles are candidate AGB stars, reddening vectors for $A_V = 30$ mag based on the extinction laws of Weingartner & Draine (2001) and Indebetouw et al. (2005) are shown as open and filled arrows, respectively, and black crosses give typical photometric errors.

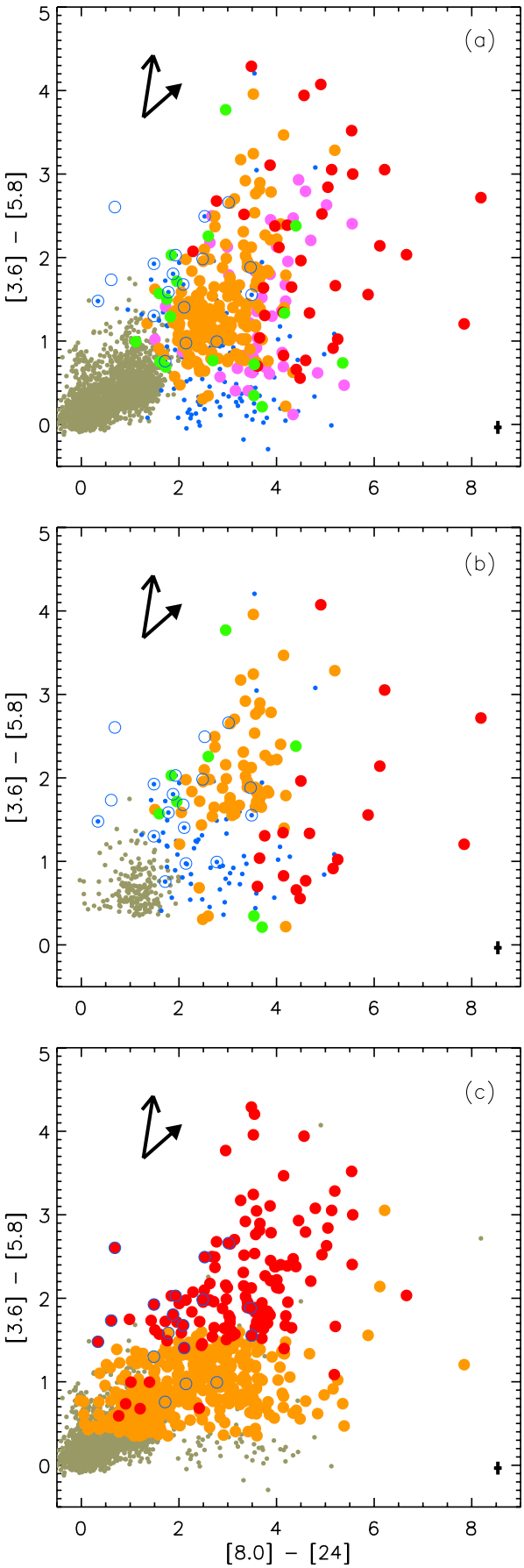

Figure 5. Same as Figure 4, except a color space combining IRAC with MIPS [24] photometry is shown.

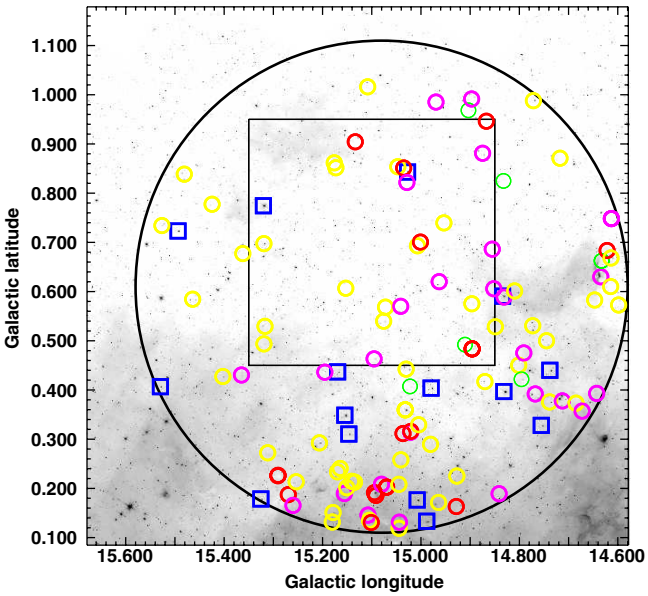

Figure 6. GLIMPSE 8.0 μm image of the control field, with the same color overlays as in Figure 3. The area searched for YSOs is shown by the black circle. The control subregion chosen to mirror the position of M17 about the Galactic mid-plane is the boxed area, 0.°5 on a side.

brightest magnitude plotted in Figure 7 is magnitude 8, because nonlinearity begins to affect the [4.5] band for brighter sources. The source density of all AGB types brighter than magnitude 8 is more than twice the density of comparably bright sources selected for our YSO sample, even before suspected AGB candidates are removed (dashed curves in Figure 7). While the brightest AGB stars will saturate the IRAC detectors and hence not be extracted into the point-source Archive, there are too few such sources visible in the target and control fields to account for a significant number of the AGB stars predicted by the Sky model. While most AGB stars in the inner Galaxy will be in the GLIMPSE Archive, evidently not all types of AGB star have large IR excesses that allow them to be confused with YSOs.

Removing suspected AGB stars from the control field sample cut the cumulative source density at magnitude 8 by more than half (the difference between the dashed and solid red curves in the right panel of Figure 7). As the cumulative source density with magnitude plotted in Figure 7 shows, the Sky model predicts that $<30\% = (70\,\mathrm{deg}^{-2} - 50\,\mathrm{deg}^{-2})/70\,\mathrm{deg}^{-2}$ of O-rich AGB stars (blue curves) and virtually no carbon stars (green curves) are fainter than [4.5] = 8 mag. Suppose that *all* the IR excess sources remaining in the control sample brighter than [4.5] = 8 mag are O-rich AGB stars, with *no* fainter AGB stars having been removed. Scaling down the *black* curve to match the solid red curve at 8 mag in the control field plot of Figure 7 shows that the final control sample could still contain up to 15 AGB stars deg^{-2}, or $\sim$12% of the overall source density ($\sim$125 deg^{-2}; value of the solid red curve at [4.5] = 14 mag). This represents the *maximum* possible fraction of AGB stars remaining in the control sample of candidate YSOs. The fraction of AGB stars remaining in the M17 target sample will be even lower ($\sim$7%), because the overall source density is 1.7 times higher (Table 1).

There remains some potential contamination from unresolved PNe. According to the predictions of the Sky model (Figure 7), these represent $<$ 10% of sources in the control sample and $<$ 5% of sources in the target sample.

We conclude that the majority (>80%) of sources selected as candidate YSOs in the control field are actual YSOs, albeit at unknown distances. This is higher than the 60% fraction of YSOs found in the recent catalog of dusty red sources in GLIMPSE compiled by Robitaille et al. (2008). This catalog contains only sources with [8.0] > 10 mJy. Virtually all Galactic AGB stars meet this brightness criterion, but only $\sim$50% of the sources in our control sample do. Therefore, if we apply the [8.0] cut of Robitaille et al. (2008) to our control sample, the fraction of candidate evolved stars *doubles*, from 20% to 40%, in good agreement with the new red source catalog despite the small size of our control sample.

The density of IR excess sources drops noticeably across the 1° increase in Galactic latitude on either side of the mid-plane (Figures 3 and 6). This suggests that star formation, in the form of isolated YSOs or small clusters, is distributed throughout the Galactic plane with a low scaleheight. The number of candidate YSOs in the M17 vicinity represents a significant enhancement over this Galactic background YSO population, as we discuss in the following section.

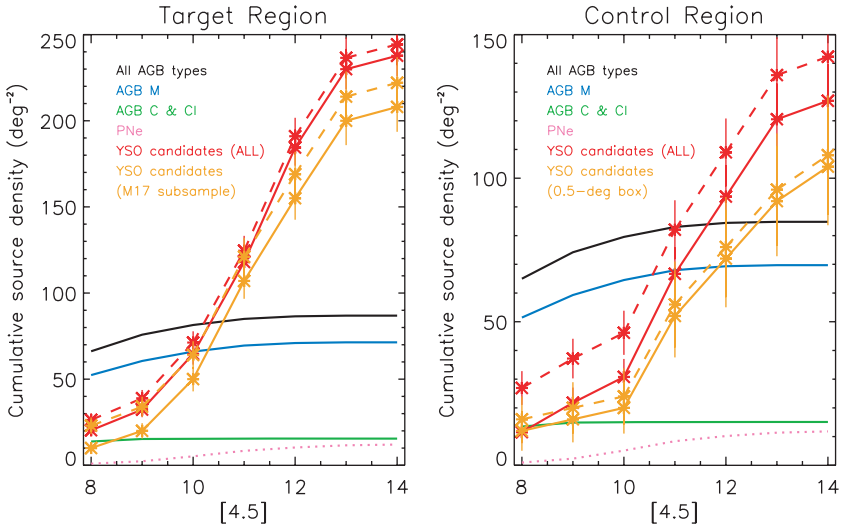

Figure 7. Cumulative densities of different types of red sources as a function of [4.5] magnitude. The curves for AGB stars (AGB M are O-rich and AGB C & CI are optically visible & obscured C-rich AGB stars, respectively) and PNe were generated by the Sky model (Wainscoat et al. 1992; Cohen 1993). The solid YSO curves represent the target and control samples and subsamples, while the dashed curves show the solid curves before bright candidate AGB stars were removed.

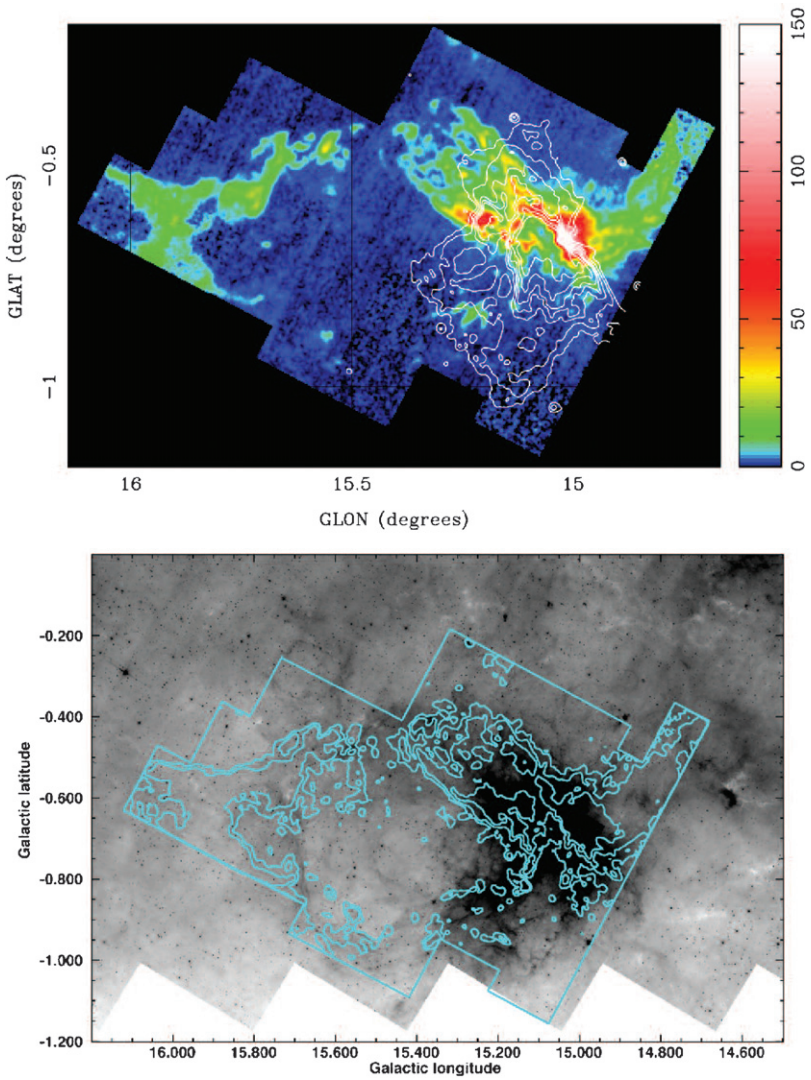

Figure 8. CO maps of extended molecular cloud structures associated with M17. Top: HHT ^{13}CO moment 0 map for v = 12–26 km s^{-1}. The image colorbar is in units of K($T_A^\star$) km s^{-1}. Contours show 90 cm continuum observations from the VLA (at intervals of 5, 10, 20, 30, 40, 60, and 80% of the map peak) that trace thermal emission from ionized gas associated with the M17 H II region. Bottom: GLIMPSE 8 μm image. Contours show HHT ^{12}CO emission at v = 19 km s^{-1}.

4. THE EXTENDED YSO POPULATION AND MOLECULAR CLOUD STRUCTURE OF M17

A ^{13}CO zero moment map for v = 12–26 km s^{-1} and a ^{12}CO channel map at v = 19 km s^{-1} are compared to the 8 μm image of the M17 target field in Figure 8. The ^{12}CO and ^{13}CO maps from the HHT reveal the underlying structure of the molecular gas outlining the extended regions of M17 along with M17 EB and portions of MC G15.9−0.7. M17 EB is a coherent, albeit clumpy, kinematic structure in molecular gas at v = 19 km s^{-1}. The CO data thus confirm that the entire dust shell observed in the IR has a common velocity with M17, supporting our conclusion that M17, M17 EB, and MC G15.9−0.7 are all part of the same dynamical complex.

M17 EB, as a bubble, should exhibit a three-dimensional, roughly spherical structure. Many astrophysical shell structures exhibit a ring-like morphology in optically thin emission due to limb-brightening, and emission from the interior of the ring may be difficult to detect. Integrating the ^{13}CO data cube spatially over a 17′ × 11′ box centered at (l, b) = (15.°6, −0.°7), we definitively detect an emission line near v = 20 km s^{-1} with a peak at $\langle T_B \rangle$ = 0.05 K. The line does not exhibit the double-peaked profile of an expansion signature, which means that if the bubble is still expanding, the expansion velocity is low, less than a few km s^{-1}, and the line profile is dominated by internal motions within the shell.

4.1. Correction for Contamination from Unassociated Sources

We have claimed that the control field sample of candidate YSOs mirrors the population of unassociated sources contaminating the M17 target field sample. We can use the control sample to remove contaminants statistically from the target sample, but first we must verify this claim. The molecular cloud complex associated with M17 contributes a significant enhancement to the gas column density in the target field with respect to the control field. This additional source of interstellar extinction could bias the source selection between our flux-limited samples.

4.1.1. Extinction Map

To estimate the extinction through the molecular cloud, we employ a model for CO line excitation based on an escape probability formalism for the CO line radiation (Kulesa et al. 2005). The observed ^{12}CO and ^{13}CO (J = 2 → 1) line intensities, velocity widths, and peak brightness temperatures

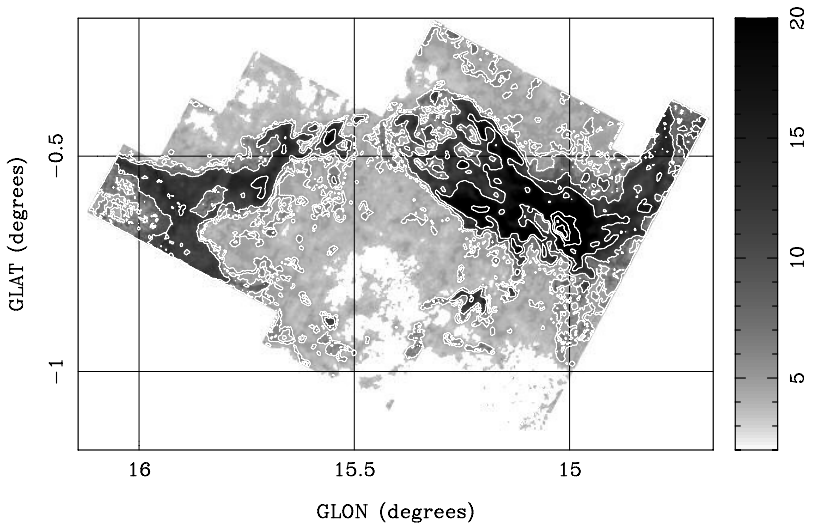

Figure 9. Extinction map produced from CO at $v = 12$–26 km s^{-1}. Gray scale is labeled in magnitudes of A_V. Contour levels are A_V of 5, 10, 15, 30, 60, and 90 mag.

constrain the model at each map pixel to give the total CO column density, N(CO), and the mean gas kinetic temperature, $\langle T_{\rm kin}\rangle$. We estimate the mean H_2 density, $\langle n(H_2)\rangle$ from the derived $N(^{13}{\rm CO})$ column density. $\langle n(H_2)\rangle$ varies from 10^3 cm^{-3} in the extended cloud structures to 10^5 cm^{-3} in the M17 South core near the H II region. The derived N(CO), $\langle n(H_2)\rangle$, and $\langle T_{\rm kin}\rangle$ are then applied as constraints on a CO PDR model based on van Dishoeck & Black (1988) to estimate the far UV radiation field, G_o, incident on the molecular gas, and the total hydrogen column density $N({\rm H}) = N({\rm H}^0) + 2N({\rm H}_2)$ (H-atoms cm^{-2}). The corresponding extinction A_V, is calculated from N(H) using the value $N({\rm H})/A_V = 1.9 \times 10^{21}$ cm^{-2} mag^{-1} (Bohlin et al. 1978). Our analysis thus attempts to incorporate the variations in both gas density and the far UV radiation throughout the cloud complex. The resulting distribution of extinction is shown in Figure 9, as a map of A_V over the region mapped in ^{12}CO and ^{13}CO.

The PDR model outputs the total hydrogen column density used in the extinction calculation. Abundances measured from the M17 H II region give $X = 0.698$ (Carigi & Peimbert 2008), and including unobserved He and metals the entire region mapped by HHT contains $1.35 \times 10^5 M_\odot$ total gas mass in the velocity range occupied by M17.

The extinction map in Figure 9 represents the *differential* extinction between the target and control fields due to the molecular and atomic gas associated with M17. The molecular gas occupies less than half of the image area, while candidate YSOs are found throughout (Figure 3). Much of the M17 molecular cloud has $A_V \gtrsim 15$ mag, reaching $A_V > 90$ mag in the dense core of M17 South. The extended outer regions of M17 and MC G15.9−0.7, however, produce $A_V < 15$ mag. This corresponds to $A_K < 2$ mag and $A_{[4.5]} < 1$ mag (Indebetouw et al. 2005) generally, and much less through the interior of M17 EB and other areas lacking high-density molecular gas. The map in Figure 9 represents the spatial average of A_V over each beam. Hence the extinction could be higher along localized sightlines through compact, dense clumps of molecular gas that are smaller than the 32″ (FWHM) resolution of our map (0.33 pc at 2.1 kpc), but such clumps occupy an insignificant fraction of the mapped area. We thus do not expect the differential extinction between the target and control fields to produce a significant disparity in mid-IR point source detections, except in the M17 molecular cloud itself.

The M17 molecular cloud and PDR do create significant, spatially varying extinction and, more importantly, produce bright diffuse mid-IR emission that saturated the MIPSGAL 24 μm images and drastically reduced the point-source sensitivity of GLIMPSE. The surface density of GLIMPSE Archive sources is 14% higher in the control field than in the target field. Much of this discrepancy is due to the sharp drop in source detections near the M17 H II region and molecular cloud, which occupy ∼10% of the area in the target field. We therefore consider the control field ill-suited for comparison with the central regions of M17, but for the remaining 90% of our extended target field the control sample gives an accurate picture of the contamination to the target YSO sample.

4.1.2. Selection of YSOs Associated With M17

The prevalence of candidate YSOs distributed throughout the M17 target field requires that a distinction be drawn between areas that are likely dominated by sources associated with M17 and external star formation regions. Using the distribution of 8 μm emission along with the CO velocity structures revealed by our HHT data, we defined a subregion of the target field that is dominated by molecular gas associated with M17 (area bounded by white in Figure 10). The 195 candidate YSOs within this region make up the M17 target subsample (Table 1). This subsample is directly comparable to the control subsample found within the boxed region in Figure 6.

In Figure 10, the background contamination to the YSO sample has been statistically subtracted such that only candidate YSOs exhibiting a significant degree of clustering are plotted. This was accomplished using a simple "friends-of-friends" nearest-neighbors analysis. We first computed the median angular separation $\theta_{\rm con}$ between each source in the control field sample and its N nearest neighbors, where $3 \leqslant N \leqslant 10$. We then calculated $\theta_{\rm targ}$, the corresponding nearest-neighbors separation for each of the candidate YSOs in the target sample. The median value of $\theta_{\rm con}$ for all sources in the control sample is $\Theta_{\rm con}$. Finally, we selected the subset of sources in the target field for which $\theta_{\rm targ} < f\Theta_{\rm con}$. The factor f comes from the ratio of surface densities between the target subsample and the control subsample ($f \equiv [\Sigma_{\rm con}/\Sigma_{\rm targ}]^{0.5}$), with $f = 0.7 \pm 0.1$ using the values from the bottom row of Table 1 and assuming counting statistics. We found that the subset of candidate YSOs selected

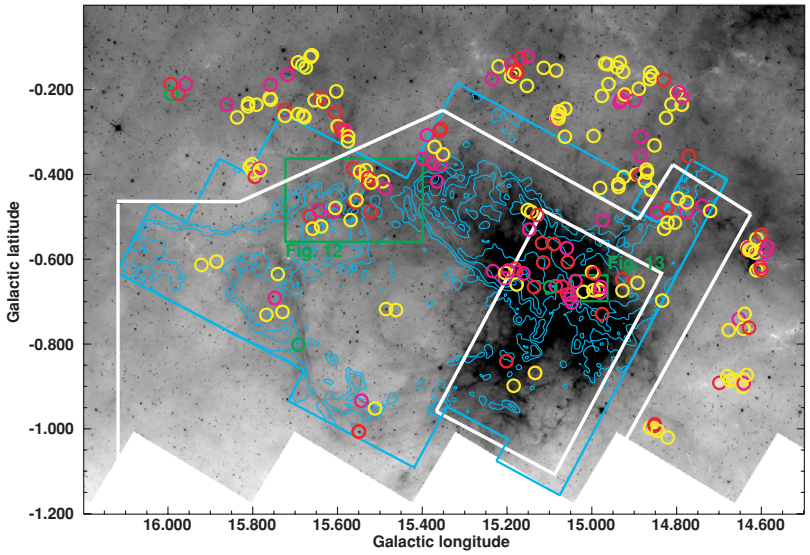

Figure 10. Candidate YSOs exhibiting significant clustering (see text). Circles mark YSO positions and are color-coded according to evolutionary stage as in Figure 3. The 8 μm image and CO contours are the same as in Figure 8 (bottom). The thick white boundary lines enclose the CO emission and pass through breaks in the spatial distribution of YSOs. The thick white rectangle shows the field that has been observed by *Chandra*, within which bright diffuse mid-IR background emission severely affects the IRAC point-source sensitivity. Green rectangles show the fields enlarged in Figures 12 and 13.

by this procedure was generally insensitive to the choice of N for $N > 3$, while the uncertainty in f creates a ~20% uncertainty on the total number of sources selected. The final sample of candidate YSOs shown outside the white rectangle in Figure 10 was selected using $N = 5$, for which $\Theta_{\rm con} = 4'.28$. For the central parts of M17 we did not correct for contaminants because our control field is unsuitable, as noted above. The 34 candidate YSOs found within the white rectangle in Figure 10 are presented in Table 4. Excluding these 34 sources, we have discarded $197/372 = 0.47$ of the sources from the original target sample. Given that we expect a fraction $f^2 \sim 100/205 = 0.49$ of the sources in the target sample to be contaminants (Table 1), our cluster-finding procedure has succeeded in removing the expected contamination.

After correcting for contaminants the final M17 YSO subsample contains 96 sources (Tables 2 and 4). Two main concentrations of candidate YSOs within the final subsample are apparently associated with M17 EB and the M17 H II region, respectively (Figure 10). The final subsample excludes 135 candidate YSOs (Table 3) that either are unassociated with M17 or are associated with the extended molecular cloud complex to the southwest (Elmegreen & Lada 1976; Sanders et al. 1986). YSOs in the latter group are at the same distance as M17 and are associated with the M17 complex, but they belong to an additional extended YSO population that is beyond the scope of this work.

4.2. Star Formation in M17 EB and MC G15.9−0.7

4.2.1. YSO Mass Function

We constructed a mass function for the observed YSO population following a procedure employed previously by Shepherd et al. (2007) and Whitney et al. (2008). Using Equation (2), we assigned a χ^2-weighted probability for the stellar mass $M_\star$ of each well-fit model to a given candidate YSO. By summing over the probabilities of all well-fit models (defined by Equation 1) and normalizing to unity, we derived a probability distribution of $M_\star$ for each candidate YSO. This procedure is similar to that employed to find the probability distributions of evolutionary stage (Section 3.1), but a finer binning was used. Results of fitting models to 62 sources in the extended M17 region (within the white boundary lines in Figure 10 but excluding the white rectangle) are presented in Table 2. Ranges giving 95% confidence intervals for $M_\star$ and $L_{\rm TOT}$ (total bolometric luminosity, including luminosity produced by accretion) for each candidate YSO are listed in Table 2. Summing the probability distributions of $M_\star$ over the 62 sources in Table 2 produces the YSO mass function (YMF) plotted in Figure 11.

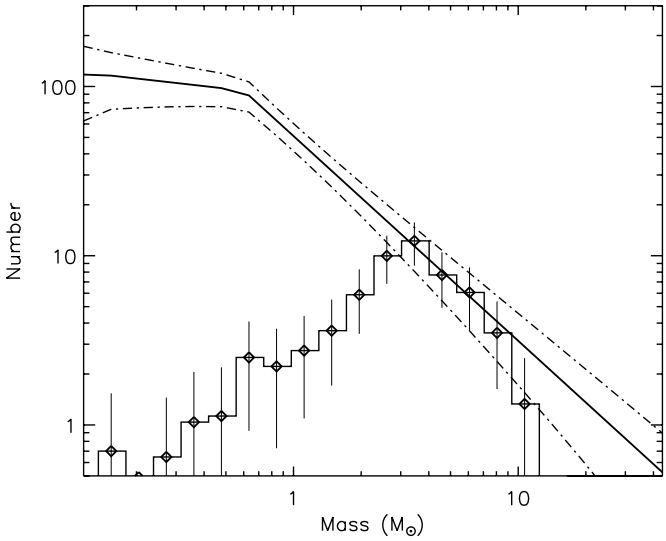

Figure 11. Mass function of the 62 candidate YSOs found inside the white boundary lines but outside the white rectangle in Figure 10 (histogram with error bars). The Orion Trapezium cluster IMF (Muench et al. 2002) has been scaled to match the mass function for ~3 $M_\odot < M_\star < 8\ M_\odot$ (heavy curve with dash-dotted curves showing uncertainty envelopes).

The YMF in Figure 11 exhibits, for intermediate-mass sources, the ubiquitous Salpeter (1955) power-law slope. The turnover for $M_\star \lesssim 3\ M_\odot$ is not a real break in the YMF but instead reflects the incompleteness of our YSO sample with

respect to the detection of lower-mass sources. A completeness limit of $\sim 3\ M_\odot$ is reasonable for the detection of disk-dominated sources. The [8.0] flux density of an A0 V photosphere with $M_\star = 3.2\ M_\odot$, $T_{\rm eff} = 10{,}800$ K, and $R_\star = 2.5\ R_\odot$ (Cox 2000) at 2.1 kpc is 3.9 mJy, or $\sim$1 dex above the nominal detection limit of the point-source Archive. The extended M17 field from which the YMF has been sampled exhibits neither high source confusion nor very bright diffuse 8 μm emission, hence our YMF represents a nearly complete sample of intermediate-mass IR excess sources that will become main-sequence types A0 or earlier.

We estimated the size of the larger YSO population represented by our intermediate-mass YSO sample by scaling the IMF of Muench et al. (2002) to fit the part of our YMF ($3 \lesssim M_\star \lesssim 8\ M_\odot$) where it is most complete (solid curves with dash-dotted uncertainty envelopes in Figure 11). This procedure generated a model IMF, $\xi(M_\star)$, for the YSO population. $\xi(M_\star)$ has a power-law slope of $\Gamma = -1.2 \pm 0.2$, as defined by

$$M_\star^\Gamma \propto \frac{d\xi(M_\star)}{d(\log M_\star)},$$

for $M_\star > 0.6\ M_\odot$. After the break point, $\xi(M_\star)$ flattens to $\Gamma = -0.2 \pm 0.2$. Although the full Muench et al. (2002) IMF is a 4-part power law extending to brown dwarf masses, we use only $\xi(M_\star \geqslant 0.1\ M_\odot)$ for consistency with the BFT07 results[15] (see Section 4.3 below). Integrating $\xi(M_\star \geqslant 0.1\ M_\odot)$, we predict that the extended YSO population of M17 numbers 950 ± 90 and represents a total stellar mass of $750 \pm 50\ M_\odot$. *These values are lower limits.* We cannot be certain that our final YMF is 100% complete even for intermediate-mass sources. We treat any unresolved multiple sources as single YSOs, which means that we are generally sensitive only to the most luminous component of a multiple system, given that $L_{\rm TOT} \propto M_\star^\alpha$, with $\alpha > 2.5$ for PMS stars (Bernasconi & Maeder 1996). The mass determined from the YSO fits will be slightly higher than the most massive source in the beam but substantially lower than the combined mass of the sources (Whitney et al. 2008).

The YMF in Figure 11 contains candidate YSOs distributed throughout a large volume of space that cannot be regarded as members of any single cluster. The YMF is, however, drawn from a coeval stellar population comprising the most recent generation of star formation in the extended M17 target field (excluding YSOs associated with the central NGC 6618 cluster). Because these sources were selected on the basis of mid-IR excess emission, and a negligible fraction were fit with Stage III YSO models, the YMF population is characterized by optically thick circumstellar disks and/or infalling envelopes. The disk destruction timescale is a decreasing function of the mass of the central star, with solar-mass YSOs losing their disks on timescales of $\lesssim$2 Myr (Haisch et al. 2001a). The intermediate-mass YSOs dominating our sample are expected to evolve more quickly, making them even younger.

4.2.2. Timescales of Evolutionary Stages and Lower Limit on Star Formation Rate

The duration of the Class I phase for YSOs in low-mass star formation regions is $\sim$0.1 Myr (Kenyon & Hartmann 1995; Haisch et al. 2000). We can make an independent estimate of the duration of the Stage 0/I phase from the accretion ages of the well-fit models for each source. We define "accretion age" as $t_A = 10^{-6} M_\star / \dot{M}_{\rm env}$ (Myr). The accretion age is a proxy for the evolutionary age t of a YSO, assuming both that $\dot{M}_{\rm env}$ is constant, on average, over t_A and that all of the accreting gas eventually reaches the central star. In reality, average accretion rates decrease with time, causing t_A to overestimate t, but accretion-driven outflows prevent 3–30% of the infalling gas from accreting (Richer et al. 2000), driving t_A in the opposite direction. Combining the probability distribution of t_A for the 25 candidate Stage 0/I YSOs in Tables 2 and 4, we find that t_A has a median value of 0.075 Myr, in good agreement with other estimates of Class I lifetimes.

Assuming a steady rate of star formation, the relative number of Stage II versus Stage 0/I YSOs gives the relative lifetime of each stage. But we must take care to compare populations with similar mass distributions. Most YSOs fit by Stage I models have steep, Class I spectral indices, and even low-mass Stage 0/I YSOs can be bright in the mid-IR. Consequently, Stage 0/I sources disproportionately populate the YMF for $M_\star < 3\ M_\odot$ (Figure 11), with the 12 Stage 0/I candidates in the YMF (Table 2) overrepresented at $1\ M_\odot \lesssim M_\star \lesssim 2 M_\odot$ compared to Stage II candidates. For $M_\star \gtrsim 3\ M_\odot$, the YMF contains 5.6 times as many Stage II as Stage 0/I candidates, while this ratio is 2.6 for the entire mass range. The median Stage II disk lifetime in our sample is therefore $t_D = 5.6 t_A \sim 0.4$ Myr. The above calculations exclude the single Stage III candidate and 18 candidate YSOs with ambiguous Stage determinations in Table 2. Nearly all of the ambiguous candidates have model fits that are divided between Stage 0/I and Stage II models. In the limiting case where all ambiguous sources are treated as Stage II candidates, we have $t_D = 8.2 t_A \lesssim 0.6$ Myr. Intermediate-mass YSOs therefore lose their disks in less than half of the corresponding $\sim$1 Myr timescale observed for their solar-mass counterparts. This age differential tends to steepen the slope of the YMF compared to a disk-unbiased IMF, hence *the intermediate-mass YMF probably underestimates the true number of low-mass YSOs.*

The characteristic age of the source population in the YMF is $t_A + t_D \sim 0.5$ Myr. Using the stellar mass estimated from the IMF model, we arrive at a star formation rate (SFR) of $0.0016\ M_\odot {\rm yr}^{-1}$ in the extended target field, which applies to M17 EB and the extended outer regions of the M17 molecular cloud. Due to the potential incompleteness and the bias against diskless sources inherent in the intermediate-mass YMF, this value must be regarded as a lower limit.

4.2.3. Triggered Star Formation in MC G15.9−0.7?

A concentration of star formation activity is observed in the vicinity of an IR dark cloud (IRDC) complex centered at $(l, b) = (15\overset{\circ}{.}55, -0\overset{\circ}{.}45)$. This region is shown in a composite GLIMPSE and MIPSGAL image in Figure 12. The bright, filamentary 8 μm emission slicing diagonally through this image, part of which makes up a previously identified optical reflection nebula, outlines the rim of M17 EB where it intersects MC G15.9−0.7 (Figure 1). Because significant concentrations of candidate YSOs are observed on the bubble rim while no group of candidate YSOs is reliably detected in the adjacent regions of MC G15.9−0.7 (Figure 10), the situation is strongly suggestive of star formation triggered by the expansion of M17 EB. The morphology of the IRDCs, bright 8 μm emission, and CO emission provides evidence for increased gas density resulting from the compression of the cloud.

[15] Extrapolating down to the hydrogen-burning limit at 0.08 $M_\odot$ increases neither the total number of YSOs nor the total stellar mass by a significant amount.

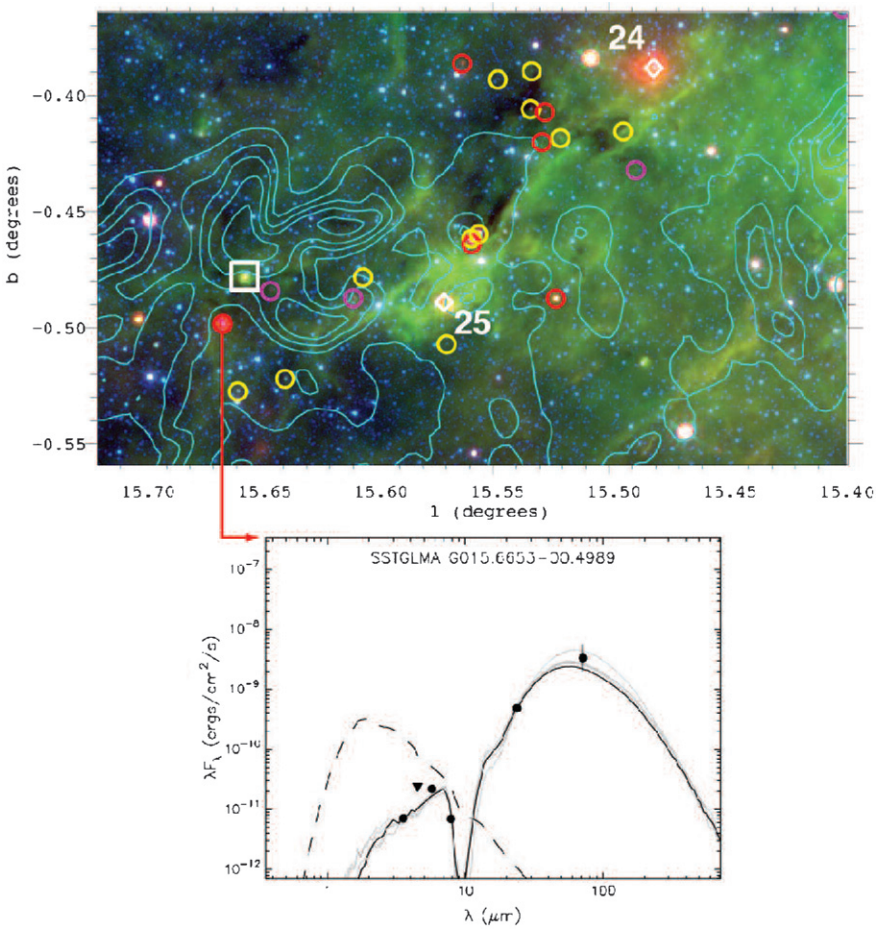

Figure 12. Image showing part of the interface between M17 EB and MC G15.9−0.7 (IRAC [4.5] = blue, IRAC [8.0] = green, MIPS [24] = red). The *cyan* contours are ^{12}CO emission at $v = 19$ km s^{-1}. The rim of the bubble M17 EB is delineated by the bright green filament of 8 μm emission crossing from the lower left to the upper right corner of the image. Candidate YSOs are overplotted as in Figure 10. Two candidate OB stars associated with diffuse 24 μm emission are marked by white diamonds and numbered as in Table 5. The candidate Stage 0/I YSO G015.6653−00.4989 (E55 in Table 2) is highlighted, and the model fits to its SED are plotted. The [4.5] flux was used as an upper limit to the fitting and is plotted as a triangle. The *dashed* curve shows the reddened photosphere of the central star as it would appear in the absence of circumstellar material.

The SED of G015.6653−00.4989, a bright 24 μm source in MC G15.9−0.7 (Figure 12), is very similar to the SEDs of several massive protostars associated with molecular outflows identified by Shepherd et al. (2007). It is characterized by excess emission at 4.5 μm (an outflow signature) and a very red IR spectral index peaking near 70 μm (this object is the brightest 70 μm point source detected in the M17 target field). The models fit to this source (E55 in Table 2) indicate a luminous candidate protostar with mass 7 $M_\odot \leqslant M_\star \leqslant 8\ M_\odot$ and luminosity 400 $L_\odot \leqslant L_{\rm TOT} \leqslant 10^3\ L_\odot$ accreting from its circumstellar envelope at a high rate of $2 \times 10^{-4}\ M_\odot {\rm yr}^{-1} < \dot{M}_{\rm env} < 8 \times 10^{-4}\ M_\odot\ {\rm yr}^{-1}$. The accretion age of this candidate protostar is $t_A < 0.04$ Myr.

A nearby resolved, compact, red IR source (in the white box in Figure 12) is associated with a second 70 μm point source. The SED of this source cannot be fit well by any YSO model, and we speculate that it may be either a luminous binary YSO or a compact cluster. Both sources are apparently located in the cloud region compressed by M17 EB.

Also shown in Figure 12 are two compact, resolved sources of 24 μm emission (30″–60″ in size) that are not associated with any candidate YSO. This emission suggests a localized region of heated dust, and the most likely heat source is a massive young star or cluster. Five such 24 μm sources are observed in the M17 target field, and none are found in the control field. At the center of every 24 μm source lies a GLIMPSE Archive source with an SED consistent with a hot stellar photosphere. Following the method pioneered by Watson et al. (2008), we estimated the spectral types of these stars by employing the RW07 model fitting tool to fit Kurucz (1993) stellar atmospheres (including hot photospheres up to $T_{\rm eff} = 50{,}000$ K) to available $BVJHK_S$+IRAC photometry. We found that all of the stars associated with compact 24 μm emission have luminosities consistent with B or late O stars, assuming they are associated with M17 at either a distance of 1.6 kpc or 2.1 kpc (see Table 5). Because these stars exhibit little or no IR excess emission in the 2MASS/GLIMPSE bands, they either have already cleared out the inner regions of their circumstellar disks or have dissipated their disks entirely. The observed 24 μm emission could arise from remnant disk material or heated dust in the surrounding molecular cloud at distances of $\sim$2–5 $\times$ 10^4 AU from the central star. This interpretation suggests that some of these stars may ionize low-luminosity compact H II regions that have not been detected by previous surveys (e.g., Wood & Churchwell 1989). None of these sources is detected by the high-resolution CORNISH survey at 6 cm (Purcell et al. 2008), indicating that any gas ionized by these B stars is diffuse enough to be resolved out by the VLA in the B configuration. This rules out the presence of hypercompact or ultracompact H II regions around the stars. The most extended of these 24 μm sources, associated with star 24 (Figure 12, Table 5), is associated with 11 cm radio

Table 5
Selected OB Stars Associated with M17

Index No.[a]	Name[b]	l (deg)	b (deg)	Cataloged Sp. type[c]	Spectral Type from SED $d = 1.6$ kpc	Spectral Type from SED $d = 2.1$ kpc	A_V (mag)
			O Stars in NGC 6618				
1,2[d]	CEN 1a,b	15.0562	−0.6884	O4+O4 V	...	...	...
3	CEN 43	15.0533	−0.7045	O3–O5 V	O4–O5 V	O5+O5 V	12.3
4	CEN 2	15.0731	−0.7004	O5 V	O5.5 V	O5.5+O7 V	5.2
5	CEN 37	15.0559	−0.6883	O3–O6 V	...	...	...
6	OI 345	15.0110	−0.7020	O6 V	...	...	...
7	CEN 18	15.0812	−0.6569	O6–O8 V	O6 V	O6+O7.5 V	7.6
8	M17-S3	15.1032	−0.6487	...	O7 V	O5 V	11.2
9	CEN 25	15.0673	−0.6879	O7–O8 V	O9 V	O6.5 V	8.0
10	OI 352	14.9945	−0.7486	O8 V	O5.5+O5.5 V	multiple[e]	∼7
11	OI 174	15.1325	−0.5257	O9 V	O6 V	O4 V or O6+O7 V	7.0
12	CEN 3	15.0658	−0.7084	O9 V	O7 V	O5 V or O7+O7 V	3.7
13	CEN 16	15.0748	−0.6460	O9–B2 V	O9.5–B0.5 V	O8 V or B0+B0 V	5.9
14	CEN 61	15.0594	−0.6884	O9–B2 V	O9 V	O6.5 V or O9.5+O9.5 V	9.9
15	CEN 27	15.0433	−0.6950	O9 V	B1 V	O9 V	∼9.5
16	CEN 31	15.0759	−0.6534	O9.5 V	...	...	...
			Candidate OB Stars in NGC 6618PG				
17	BD-16 4831	15.3213	−0.7758	O+	O5.5 V or O9 III	O4 V or O7 III	4.4
18[f]	BD-16 4826	15.2604	−0.7263	O5	O5.5 V or O9 III	O5 V or O6.5 III	3.9
19	BD-16 4822	15.2244	−0.6796	B...	O8.5 V	O6.5 V	2.9
20	TYC 6265-1174-1	15.1882	−0.7598	B0	B1 V	O9 V	3
21	HD 168585	15.2855	−0.7498	B7–B8 II	B1 V	O9 V	1.6
			Candidate OB Stars Associated with 24 μm Emission in M17 EB				
22[g]	ISOGAL YSO	15.3320	−0.7174	...	late B V	B1.5 V	2.1
23[h]	TYC 6265-347-1	15.3583	−0.6543	O...	B2 V	B1 V	2.6
24	BD-15 4928	15.4801	−0.3889	B	B0.5 V	O8 V	2.8
25		15.5702	−0.4895	...	B1 V	B0.5 V	∼4.8
26	TYC 6265-2079-1	15.5900	−0.8268	O...	B4 V	B2 V	1.7

Notes. All O stars in NGC 6618 are *Chandra* point sources (BFT07). The only star in NGC 6618PG that has been observed by *Chandra*, No. 20, is also an X-ray point source.

[a] OB stars in each of the first two groups are listed in order of decreasing luminosity, while the candidate B stars in the final group are listed in order of increasing Galactic longitude.

[b] CEN is Chini et al. (1980), and OI is Ogura & Ishida (1976). SWB M17−3 is a recently discovered O star driving a stellar wind bow shock (Povich et al. 2008). Other identifiers are from SIMBAD.

[c] Spectral types for NGC 6618 are from OI, CEN, Hanson et al. (1997), and Hoffmeister et al. (2008); others are from SIMBAD.

[d] CEN 1a,b refer to the main components of an apparent O4+O4 visual binary that are saturated and marginally resolved by IRAC. CEN 1a,b each are spectroscopic binary systems with nearly equal-luminosity components (Hoffmeister et al. 2008).

[e] At 2.1 kpc, the SED fits to OI 352 return a radius larger than that of an O supergiant. It may be an unresolved multiple O system (see text).

[f] BD-16 4826 is a *ROSAT* point source (Dunne et al. 2003).

[g] This source, ISOGAL-P J182108.8−155658 from the catalog of Felli et al. (2002), exhibits a marginal IR excess at 5.8 μm and is not detected as a point source at 8.0 μm.

[h] This source exhibits an IR excess at 8 μm.

emission (Reich et al. 1990) and enclosed by a partial ring of 8 μm emission at a projected distance of 0.5 pc from the star, suggesting a small H II region and PDR.

Whatever the interpretation of the physical origin of the 24 μm sources, the circumstellar environments of the associated OB stars are significantly more evolved than those of the candidate YSOs, which exhibit IR excess emission at wavelengths <10 μm. The comparison of star 25 with YSO E55, the candidate protostar in Figure 12, is particularly interesting. These two sources have comparable masses (∼10 $M_\odot$; E55 is still gaining mass through accretion) and are apparently located within the same molecular cloud, but they occupy strikingly different phases of early massive stellar evolution, suggesting a difference in age comparable to the disk destruction timescale derived above, $t_D \sim 0.4$ Myr. This difference in age could be explained naturally by triggered star formation. The more evolved B star lies in the midst of the 8 μm emission defining the inner rim of M17 EB, while the young candidate protostar is located in a region of the molecular cloud that has only recently been overtaken by the expanding bubble. The expansion velocity of the bubble implied by this scenario is slow, a few km s^{-1} at most, which is consistent with the non-detection of an expansion signature in the CO line (Section 4 above).

4.3. The M17 Molecular Cloud and H II Region

The contours in the top panel of Figure 8 show a 90 cm Very Large Array (VLA) radio image (Brogan et al. 2006) delineating the extent of the ionized gas associated with the main M17 H II region. The densest part of the M17 molecular cloud is located in M17 South (see Figure 1) along the interface between the H II

region and the bright ^{13}CO ($J = 2 \rightarrow 1$) emission (colored red-white in Figure 8). The total gas mass (molecular and atomic) contained in the main M17 molecular cloud is $\sim 6 \times 10^4\ M_\odot$, found by integrating the column density traced by the CO emission. The H II region occupies a cavity cleared of molecular gas between M17 North and M17 South. The morphology of the CO emission from M17 closely resembles the maps of the region obtained by Wilson et al. (1999), but the older maps have slightly lower resolution and do not include M17 EB. The cavity in the molecular cloud has been sculpted by the winds and radiation of the O stars in NGC 6618 (Povich et al. 2007).

4.3.1. Prominent Massive Stars

The spectral classifications derived from SED fits to 27 prominent OB stars in the M17 target field are presented in Table 5. We fit Kurucz (1993) stellar atmospheres to the broadband fluxes of 11 of the 16 known O stars in NGC 6618 that have reliable, unsaturated fluxes in the GLIMPSE Archive to estimate their spectral types. Although all known O stars in NGC 6618 except No. 8 have previously reported spectral types from optical and near-IR spectroscopy and photometry (Ogura & Ishida 1976; Chini et al. 1980; Hanson et al. 1997; Hoffmeister et al. 2008), mid-IR photometry offers the advantage of a relatively extinction-independent determination of the luminosity in the Rayleigh-Jeans regime of the stellar SED. We incorporated available B, V photometry (Ogura & Ishida 1976; Hoffmeister et al. 2008) into each SED to obtain more reliable estimates of A_V toward each star than would be possible from the 2MASS photometry alone. Because the optical-IR SED shape does not vary significantly for stars earlier than B3, the A_V derived from our SED fitting is independent of adopted distance. As shown in Table 5, our SED-based luminosity classification at 1.6 kpc agrees with previously reported spectral types to within 2 subclasses for 8 of the O stars analyzed in NGC 6618. This might seem surprising, given that the most recent distance determination found that M17 cannot be significantly nearer than 2 kpc (Hoffmeister et al. 2008). However, previous photometric determinations of spectral type assumed that each source was a single star, and our method shares the same systematic bias with respect to distance. Even spectroscopic determinations have generally neglected multiplicity, and the resulting spectrophotometric distance estimates contributed to the wide adoption of the 1.6 kpc distance.

Revising the distance from 1.6 to 2.1 kpc multiplies the luminosity of every star in Table 5 by 1.7. This factor of $\sim$2 is suggestive. The majority of O stars in clusters have been observed to be in near-equal-mass binary systems (Sana et al. 2008; Mason et al. 2009). Hoffmeister et al. (2008) found that each component of the historical O4+O4 binary CEN 1, the most luminous star system in M17, is itself a spectroscopic binary with approximately equal-luminosity components and suggested that several other known O stars in NGC 6618 could also be unresolved binaries. Assuming the stars in Table 5 are at 2.1 kpc, we find that the majority of O stars in NGC 6618 are far more luminous in the mid-IR than expected from the cataloged main-sequence spectral types. Three of these stars, CEN 43, CEN 2, and CEN 18, each have mid-IR luminosities exceeding an O3 V star. Three others, OI 174, CEN 3, and CEN 61, are unlikely to be single main-sequence stars because their SED-derived spectral types are > 2 subclasses earlier than their cataloged spectral types (Table 5). Because NGC 6618 is very young and even O4 V stars take $\sim$4 Myr to evolve off the main sequence (Bressan et al. 1993), it is unlikely that the massive stars in NGC 6618 are giants. We therefore give binary classifications for the overluminous stars in Table 5, with spectral types estimated for each component assuming (1) that the components have nearly equal masses and (2) that their combined light yields the cataloged or SED-derived spectral type for a single star at 1.6 kpc. We stress that our spectral typing for each component of the binary systems is not definitive, but the high fraction of candidate binary systems is a robust result.

At 2.1 kpc, one source, OI 352, has mid-IR luminosity equivalent to a binary O3+O3 V system. If this were the true classification, then OI 352 would compete with CEN 1a,b for domination of the H II region, but in fact OI 352 is located in an unremarkable part of the nebula, outside the central wind-dominated cavity (Townsley et al. 2003; Povich et al. 2007). We therefore speculate that this star, like CEN 1, could be a multiple system of three or more later-type O-dwarfs. BFT07 report an unusually hard (4.4 keV) thermal component from their plasma fits to the X-ray spectrum of OI 352. Strong shocks produced by colliding-wind binaries are the most promising explanation for O stars with >1 keV hard X-ray emission. CEN 1a,b, CEN 43, CEN 2, and CEN 18 all produce hard X-ray emission (BFT07), and all are identified as candidate binaries by H08 and/or by our SED fitting, with primaries of type O6 V or earlier. CEN 25, a solitary O6.5 V star, lacks hard X-ray emission. In contrast, OI 174, CEN 3, and CEN 61 are likely binary systems with primaries of type O6 V or later, and these systems have only soft-component X-ray spectra. Evidently hard X-ray emission is not a ubiquitous property of massive binary systems, but this phenomenon may be more common in earlier-type binaries. CEN 16 seems anomalous, for although it boasts a very hard X-ray spectrum (3.5 keV), it is among the least luminous candidate O stars, equivalent to an early B binary system (Table 5).

4.3.2. Comparison of X-ray Sources with GLIMPSE YSOs

The white box in the bottom panel of Figure 10 outlines the field observed to date by *Chandra* (L. K. Townsley et al. 2010, in preparation; P. S. Broos et al. 2010, in preparation). BFT07 presented 886 X-ray point sources extracted from the first *Chandra* Advanced CCD Imaging Spectrometer (ACIS) observation of M17. By scaling the X-ray luminosity function (XLF) of the Orion Trapezium Cluster to match the XLF of the M17 sources, BFT07 estimated a total young stellar population of 8000–10,000 members (to a limiting mass of 0.1 $M_\odot$) in the NGC 6618 cluster and its immediate vicinity in M17. BFT07 assumed a distance of 1.6 kpc, and scaling their XLF to 2.1 kpc increases the total population to 11,000–14,000 stars and YSOs.

Of the 195 candidate YSOs in our M17 subsample (Table 1), only 34 fall within the $17' \times 17'$ field of the ACIS observations. This number would be many times higher if not for the presence of extremely bright diffuse mid-IR emission from the H II region and PDR that drastically reduces the point-source sensitivity in all IRAC bands. The source density in the GLIMPSE Archive within the ACIS field analyzed by BFT07 is 107,000 deg^{-2}. This is only $\sim$50% of the average density of Archive sources in the larger M17 target field (see Table 1), *despite* the fact that the ACIS field contains the dense center of the NGC 6618 cluster. Because of this incompleteness, we cannot attempt any meaningful quantification of the YSO population most directly associated with NGC 6618. X-ray observations, by contrast, do not suffer from the deleterious effects of bright backgrounds, and moreover the (near-axis) spatial resolution of ACIS is higher than that of IRAC. Because very different physical mechanisms

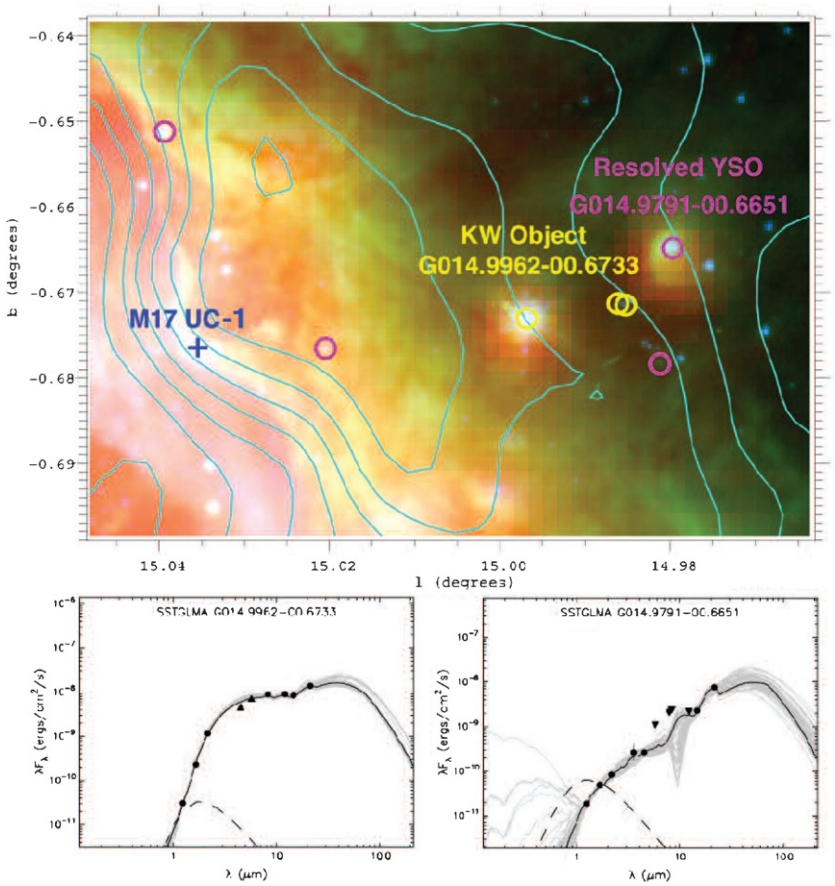

Figure 13. Region containing the peak molecular gas density in M17, near the H II region–PDR interface. The image combines IRAC [4.5] (blue) and [5.8] (green) with MSX E (21.3 μm; red). The *cyan* contours are the HHT ^{13}CO moment 0 map from the top panel of Figure 8. Candidate YSOs are overplotted as circles using the color scheme of Figure 3. The ultracompact H II region M17 UC-1 is marked. The KW Object (left) and neighboring resolved YSO (right) are also highlighted, and the model fits to their SEDs are plotted as in Figure 12. Fluxes used as upper or lower limits for the model fitting are plotted as downward- and upward-pointing triangles, respectively.

are responsible for X-ray versus IR emission from young stars, we are interested in learning whether the IR-excess sources selected for our YSO sample represent a subsample of the X-ray-selected population or a distinct population.

Preibisch et al. (2005) performed a detailed analysis of the X-ray source population observed as part of the *Chandra* Orion Ultradeep Project (COUP). They found that the 838.1-ks COUP observation detected 100% of the known young F- and G-type young stars and YSOs in Orion but only ∼50% of A-type stars. Preibisch et al. (2005) concluded that the X-ray emission observed in the low-mass stars in the COUP sample is consistent with an origin in stellar coronae analogous to the solar corona, but at a considerably higher level of activity. The disappearance of solar-type convective envelopes in more massive stars on the main sequence could explain the drop in the COUP completeness for intermediate-mass stars.[16] Preibisch et al. (2005) also observed that X-ray emission in T Tauri stars is partially suppressed by accretion. As we have shown, our IR-selected sample of candidate YSOs is highly sensitive to intermediate- to high-mass objects that are still accreting via circumstellar disks and/or envelopes. We therefore expect that our YSO sample complements the (much larger) X-ray-selected sample, as we preferentially select the YSOs that are the most likely to be missed by *Chandra*.

[16] Microshocks in OB stellar winds are believed to be the primary source of soft X-ray emission from massive stars; this very different from the emission mechanism operating in low-mass stars.

We have correlated our final YSO sample with an updated X-ray source catalog covering the entire area observed to date by *Chandra*/ACIS, with 400 ks total integration time (P. S. Broos et al. 2010, in preparation). Out of the 34 candidate YSOs in the overlap region, 14 have X-ray counterparts. The 95% confidence intervals for $M_\star$ and $L_{\rm TOT}$, along with the evolutionary stage derived from the well-fit (Equation (1)) YSO models, are given in Table 4 for each source. The sources in Table 4 exhibit no obvious trends in mass, luminosity, or evolutionary stage with which to distinguish candidate YSOs with X-ray counterparts from those without. The majority of the candidate YSOs in Table 4 are fit with models of intermediate to high stellar mass corresponding to spectral types A and B on the main sequence. There may be a slight preference for less-evolved sources with higher accretion rates in the X-ray quiet population in Table 4, but this is not significant, given the small sample size. Intrinsic X-ray variability may play a role in determining which YSOs are detected. It is also possible that some of the luminous YSOs with ACIS detections are themselves X-ray quiet but possess binary companions that are X-ray bright. *There is no evidence that the 34 candidate YSOs listed in Table 4 represent a distinct population from the X-ray-selected sources.*

Two interesting candidate massive YSOs are located near the peak molecular gas density of M17 South and the interface with the H II region, shown in Figure 13. One, the KW Object, is a binary system. A candidate Herbig Be star is the more luminous component (KW-1) and dominates the IR emission (Jiang et al.

2002; Chini et al. 2004a). The lower-luminosity component (KW-2) is X-ray bright (BFT07) but unresolved in our IR survey data, hence the KW Object is considered an X-ray detected source (X4) in Table 4. KW-1 is saturated in the GLIMPSE and MIPSGAL images, so models were fit to its 2MASS and MSX fluxes only. The model fits indicate a central star of $M_\star \sim 10\ M_\odot$ and $T_{\rm eff} \sim 26{,}000$ K, consistent with an early B star and in good agreement with the findings of Chini et al. (2004a). The models indicate that the star may have a substantial circumstellar disk ($0.01\ M_\odot \leqslant M_{\rm disk} \leqslant 0.3\ M_\odot$) with a large inner hole of radius ~40 AU (~10 times the dust sublimation radius). The inner hole is responsible for the precipitous rise in the near- through mid-IR SED (Figure 13) and indicates that the central star has ceased accreting material from the disk. Our model SEDs produce a broad 9.7 μm silicate feature in emission, but ISOCAM spectra presented by Chini et al. (2004a) show that the "bumps" in the SED near 8 and 11 μm are actually due to PAH emission features excited by the hot, central star. We have therefore used the *MSX* A and C bands as upper limits to the SED fitting, since these bands contain PAH features that increase their flux with respect to the continuum provided by the YSO models. The 1-D envelope model employed by Chini et al. (2004a) predicts the silicate feature in absorption and does not explicitly include a disk. These authors report a total circumstellar mass of 10 $M_\odot$ within 0.1 pc from the star. The total mass and envelope radius are very difficult to constrain in the absence of mm/sub-mm data, hence we cannot confirm these reported values.

The other prominent candidate YSO highlighted in Figure 13, G014.9791-00.6651, is resolved by IRAC. This source, NX5 in Table 4, is not detected in X-rays. Like KW-1, NX5 is massive ($M_\star \sim 10\ M_\odot$), but it may be somewhat less evolved. The parameters of the 47 well-fit models poorly constrain the circumstellar environment of NX5, allowing for a wide range of both $M_{\rm disk}$ and $\dot{M}_{\rm env}$, so the evolutionary stage is ambiguous, split between 60% Stage II and 40% Stage 0/I models. The resolved outer envelope of this star is large, with radius $\sim 10^5$ AU, and the SED exhibits the signatures of a PAH spectrum. As with our modeling of KW-1, we set the bands most affected by PAHs as upper limits for the model fitting, and the majority of well-fit models cluster around $T_{\rm eff} \sim 23{,}000$ K, hot enough for the star to produce sufficient UV radiation to excite PAHs in its circumstellar material. Together with M17 UC-1, the nearby hypercompact H II region that is excited by a B0 star (Sewilo et al. 2004), KW-1 and NX5 are three very luminous YSOs with very similar stellar masses but with very different circumstellar environments. This demonstrates that, in spite of their close proximity to each other, these 3 sources are not precisely coeval.

4.3.3. Challenges of Identifying Cluster Members and Determining the Age of NGC 6618

The fraction of stars exhibiting IR excess emission due to circumstellar disks is a diagnostic of the age of embedded clusters (Haisch et al. 2001b). BFT07 find that only ~10% of the sources in their X-ray selected sample exhibit IR excesses. This fraction is very low in comparison to recent results using IR-selected source samples. Jiang et al. (2002) found a *JHK* excess fraction of 53% in the central regions of the NGC 6618 cluster, and Hoffmeister et al. (2008) reported a 74% excess fraction from deeper *JHKL* observations of a similar field. Some variation in excess fraction is inevitable due to differences in sample selection, and excess fractions measured in the *JHKL* color plane are expected to be higher than those in the *JHK* color plane. The low excess fraction reported by BFT07 is partially explained by selection biases against embedded sources and against low-mass sources, both of which are fainter in X-rays. To gain depth beyond the 2MASS and GLIMPSE catalogs, BFT07 correlated their X-ray sample with SIRIUS JHK_S photometry presented by J02, hence the difference between the excess fractions reported by these two works reflects the different selection criteria and analysis techniques rather than differences in IR photometry.

The large discrepancy between reported IR excess fractions reflects a more basic issue: The M17 H II region is a difficult place to search for YSOs. The diffuse IR emission is bright at all wavelengths with a steep red spectral index and exhibits complex morphological structure on multiple spatial scales (Povich et al. 2007). This makes reliable mid-IR photometry difficult even for bright sources and impossible for faint ones. Nebular structures can be mistaken for IR excess emission associated with stars. As Povich et al. (2008) note, two of the high-mass Class I sources identified by Nielbock et al. (2001) are actually mid-IR emission from stellar-wind bow shocks that could be mistaken for circumstellar disks. Lada et al. (1991) claimed that the majority of high-mass stars in NGC 6618 display *JHK* excess, but this was disputed by Hoffmeister et al. (2008). Among the O stars in NGC 6618 detected by the GLIMPSE, all are detected at wavelengths as long as 4.5 μm and many are detected at 8.0 μm, but we can state with high confidence that none display an IR excess, with the possible exception of star No. 8 in Table 5, which is associated with a third mid-IR bow shock (Povich et al. 2008).

Near-IR photometry can be more reliable, because the diffuse emission is less bright. But *JHKL* observations are challenged by the large spatial variations in interstellar extinction across the M17 cloud (see the A_V values in Table 5, for example). While the extinction due to molecular gas in the M17 North and South cloud components is generally $A_V > 15$ mag, and the dense core of M17 South produces $A_V > 90$ mag, the average extinction through the central cavity is $A_V < 15$ mag (Figure 9). The average extinction observed toward the ionizing stars of the M17 H II region is $A_V \sim 8$ mag (Table 5; Chini et al. 1980; Hanson et al. 1997; Hoffmeister et al. 2008). The foreground extinction to the cloud is $A_V \sim 2$ mag (Pellegrini et al. 2007; Hoffmeister et al. 2008). We thus deduce that the column density of the M17 cloud is divided into approximately equal halves behind ($A_V \sim 7$ mag) and in front ($A_V \sim 6$ mag) of the H II region. Including foreground extinction, the total extinction along a typical line of sight through the cavity is $A_V < 17$ mag, or $A_K < 2$ mag. Hence background stars are detectable even in relatively shallow near- and mid-IR observations along the line of sight through the central cavity and the ionizing cluster. In contrast, adjacent dense regions of the M17 North and South cloud components produce sufficient extinction to screen out background stars against even deep near-IR observations. Because of this complex extinction morphology, there is no comparable nearby field that can be used to estimate the background contamination in observations of NGC 6618. Any attempt to measure accurately the disk fraction or low-mass IMF in NGC 6618 must overcome this significant challenge.

A major strength of X-ray observations is the ability to separate young cluster members, which are two to three orders of magnitude brighter in X-rays than older main-sequence or evolved stars, from the field star population (BFT07 and references therein). The contamination from unassociated sources in

the X-ray sample of the M17 young stellar population is therefore very low, <5% (BFT07). Jiang et al. (2002) recognized the difficulty in using their off-cluster field to correct for source contamination and instead used a Galactic disk population synthesis model. While we are not in a position to verify their results, the conservative upper limit of 3 Myr on the cluster age derived by Jiang et al. (2002) is reasonable. H08 assumed that all stars with IR excess, and by extension all sources with reddening equivalent to $A_V \gtrsim 10$ mag, were cluster members. H08 therefore concluded that the M17 molecular cloud behind NGC 6618 was opaque. Both the assumption and the conclusion were not valid. The extinction through the central cavity is relatively low ($A_K < 2$ mag) and the deep observations used by H08 detected stars as faint as $K = 20.1$ mag and $L = 15.6$ mag. The sample of H08 therefore contains a potentially large fraction of background stars, casting doubt upon the reported disk fractions and the correspondingly young age of 0.5 Myr claimed for the M17 stellar population.

It is tempting to conclude that the inclusion of diskless field stars in a magnitude-limited sample of the M17 young stellar population would decrease the measured IR excess fraction. But stars with disks are not well-separated from reddened stellar photospheres in the *JHK* or even in the *JHKL* color–color diagrams (Whitney et al. 2003b; Robitaille et al. 2006). Color–color spaces or SEDs that include photometry at 4.5 μm and longer wavelengths provide a significantly more reliable means for distinguishing circumstellar extinction from interstellar extinction. Of the 64 candidate X-ray emitting protostars identified by BFT07 (their Table 7) most of them on the basis of the $K - [3.6]$ color (analogous to $K-L$), only 3 were selected as YSOs by our more conservative multiband SED fitting (see Table 4), but 16 were well fit by reddened stellar photospheres (the remaining sources are detected in too few 2MASS/GLIMPSE bands to be fit reliably with SED models). Highly reddened contaminating sources that are intrinsically red, such as the numerous red giants in the Galactic plane behind the M17 H II region, are the most difficult to separate from YSOs on the basis of *JHKL* colors alone. If correction for contamination is not done, then highly reddened, background red giants may provide a significant number of *false* IR excess sources. This would artificially increase the derived disk fraction, leading to an underestimate of the cluster age.

We are left without a strong constraint on the age of the M17 young stellar population. There is a population of PMS stars lacking inner disks (BFT07), and there is also ample evidence for ongoing star formation (Nielbock et al. 2001; J02; this work). The preponderance of observational evidence indicates that M17 has not formed all of its stars simultaneously, but has experienced continuous or episodic star formation over a period of <3 Myr. Sources like the candidate massive YSOs and M17 UC-1 shown in Figure 13 are almost certainly younger than 0.5 Myr, the average age of the extended YSO population (Section 4.2 above). To minimize the impact of the lingering age uncertainty, we adopt a mean age of ∼1 Myr for the young stars and YSOs in NGC 6618 and the surrounding molecular cloud.

We can use the BFT07 results to make an estimate of the SFR that has produced the ionizing cluster of M17 and its entourage of YSOs. Scaling the stellar initial mass function (IMF) measured by Muench et al. (2002) for the Orion Trapezium Cluster to the 11,000–14,000 stars in M17, we arrive at a total mass in stars of 8000–10,000 $M_\odot$. Stars have been forming in M17 at an average rate of 0.008–0.01 $M_\odot \mathrm{yr}^{-1}$.

5. A HISTORY OF PROPAGATING MASSIVE STAR FORMATION

We have shown that the major sites of star formation in the extended M17 region are located around the rim of the large bubble M17 EB. We will now examine the structure and possible origins of M17 EB and show that the beginnings of a plausible star formation history of M17 are found within this bubble.

5.1. The Origin of M17 EB

The most likely production mechanisms for a bubble the size of M17 EB are the expansion of an H II region or a supernova explosion, both of which are expected to occur in regions of massive star formation. We favor the H II region interpretation. The morphology of the mid-IR emission outlining M17 EB is similar to that of other 8 μm bubbles outlining the PDRs of H II regions (Churchwell et al. 2006; Watson et al. 2008). One of the best ways to discriminate between H II regions and supernova remnants (SNRs) is by the radio continuum spectral index. H II regions are filled with thermal emission from ionized gas and exhibit a flat spectral index for optically thin radio emission, while SNRs are often characterized by steep, non-thermal spectral indices from synchrotron emission (e.g., Brogan et al. 2006). M17 EB is included in two single-dish radio Galactic plane surveys of comparable spatial resolution. Images at 3 cm from the Nobeyama 45 m telescope (HPBW = 2.′7; Handa et al. 1987) and at 11 cm from the Effelsberg 100 m telescope (HPBW = 4.′3; Reich et al. 1990)[17] show a plateau of radio continuum emission that fills the half of M17 EB farthest from M17 (other half is dominated by emission from the M17 H II region itself) and drops sharply at the location of the 8 μm emission outlining M17 EB. Comparison of the 3 cm and 11 cm surface brightnesses at various points in the interior of M17 EB shows that the radio continuum flux density is approximately constant (with a typical value of ∼50 mJy) over this wavelength range, consistent with a flat, thermal emission spectral index.

One caveat regarding the interpretation of the radio emission within M17 EB should be kept in mind. The non-thermal emission from SNRs eventually fades (on the order of a few 10^5 yr) to the point of becoming indistinguishable from the background. The residual thermal emission from the parent H II region lasts much longer. Hence, we cannot rule out the possibility that a supernova has occurred within M17 EB. But because the observed thermal radio emission completely fills the bubble, there is no need to invoke a supernova explosion to explain its origin.

A search of SIMBAD objects with coordinates inside M17 EB reveals a group of five stars with OB spectral classifications. Although a few of these stars have proper motion estimates (Høg et al. 2000), none have parallax distances. The spectral types of these sources listed in the SIMBAD database are of unknown provenance and questionable quality, so while we list the catalogued spectral types for reference in the lower two sections of Table 5, we trust the classifications only to the extent that they identify hot stars. Again following Watson et al. (2008), we fit SEDs generated from Kurucz (1993) stellar atmospheres to available *B*, *V*, 2MASS, and GLIMPSE fluxes of these stars, and we find that their IR luminosities are consistent with very early spectral types at either 1.6 kpc or 2.1 kpc (Table 5). If the stars were at a significantly different distance, their SEDs would

[17] See http://www.mpifr-bonn.mpg.de/survey.html.

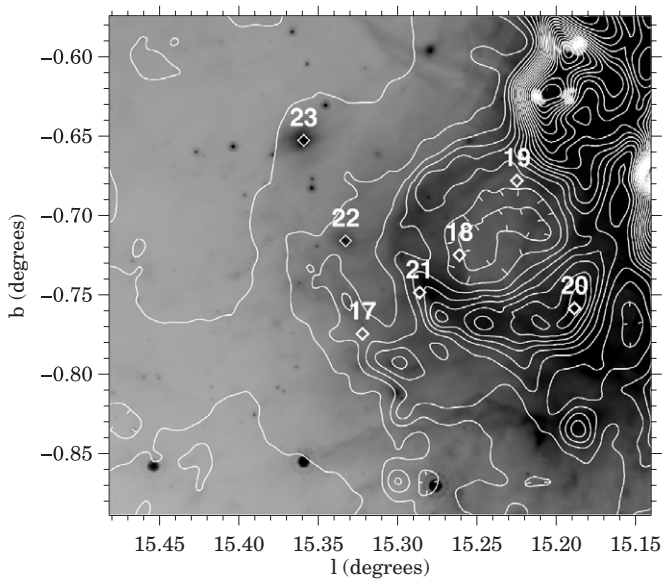

Figure 14. MIPS 24 μm image highlighting the OB stars of NGC 6618PG (heavy diamonds) and the 90 cm radio ring (contours). Two candidate B stars associated with 24 μm emission are indicated by thin diamonds. Source numbers are from Table 5.

be inconsistent with early-type stars. We therefore suggest that these stars are the five most massive members of NGC 6618PG, the ionizing cluster driving M17 EB (Figures 14 and 15).

The OB stars of NGC 6618PG are significantly less reddened ($A_V \leqslant 5$ mag) than the O stars in NGC 6618, as expected since NGC 6618PG is located in a much more diffuse H II region. NGC 6618PG is associated with both Hα emission and *ROSAT* soft X-ray emission (Dunne et al. 2003). The soft X-ray emission is also apparent in an archival *Einstein* observation taken 13 years earlier than the *ROSAT* survey. Significant differences in morphology between these two images show that the X-ray emission is variable on $\lesssim$10-yr timescales. We therefore infer that the emission is dominated by unresolved X-ray-bright point sources; these are the young stars of the NGC 6618PG cluster. High-resolution X-ray observations of the interior of M17 EB with *Chandra* or *XMM-Newton* are needed to separate individual cluster members from field stars and to detect any truly diffuse X-ray emission.

The NGC 6618PG cluster must be significantly more evolved than NGC 6618 because, even in the absence of bright diffuse mid-IR emission from the interior of M17 EB, we do not detect *any* candidate YSOs above the background level in the vicinity of the candidate ionizing stars and X-ray emission. Given that elsewhere in the target field we detect at least a few solar-mass stars with optically thick disks, the absence of candidate YSOs means that the age of NGC 6618PG is >2 Myr (Haisch et al. 2001a). We therefore consider the possibility that the OB stars have evolved off the main sequence, and list possible spectral types of luminosity class III for the most luminous stars, BD-16 4831 and BD-16 4826 (Nos. 17 and 18 in Table 5). These stars place an upper limit on the age of NGC 6618PG. Assuming negligible mass loss, an O6.5 III star spent ~4.5 Myr as an O5 V star followed by $\lesssim$0.5 Myr of post-main-sequence evolution (Bressan et al. 1993; Martins et al. 2005), for a maximum age of ~5 Myr. Stars 17 and 18 are the best candidates for ionizing the H II region inside M17 EB, although we cannot rule out the possibility that other luminous stars once contributed to the ionization and have since gone supernova.

The locations of all five candidate ionizing stars in NGC 6618PG and the surrounding interior of M17 EB are marked on a MIPSGAL 24 μm image in Figure 14. Also shown are contours of 90 cm radio continuum from VLA observations (Brogan et al. 2006). An obvious feature of this image is a ring-shaped structure, centered at $(l, b) = (15\overset{\circ}{.}23, -0\overset{\circ}{.}72)$ and ~6′ in diameter, that is apparent in both the IR and radio continuum. While this structure is superficially suggestive of a SNR, careful analysis of available VLA data at 20 cm and 90 cm combined with 3.6 cm observations from the commissioning of the 100 m Robert C. Byrd Green Bank Telescope[18] reveals that the radio spectral index is consistent with thermal emission. There is no significant difference between the spectral index of the radio ring and the rest of the M17 H II region. The 24 μm morphology is reminiscent of a stellar-wind bubble produced by a luminous

[18] See http://wiki.gb.nrao.edu/bin/view/Observing/M17publicImage.

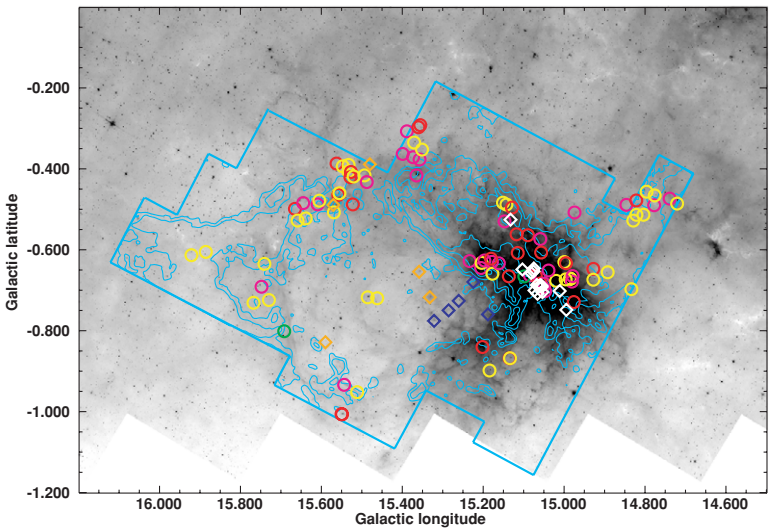

Figure 15. Overview of the extended massive young stellar population associated with M17 described in this work. *Cyan* contours of ^{12}CO emission at $v = 19$ km s^{-1} are overlaid on a GLIMPSE 8 μm image. Candidate YSOs associated with the extended M17 molecular cloud and M17 EB are marked by colored circles as in Figure 10. Diamonds mark the known O stars of NGC 6618 (white), the five most massive OB stars detected in NGC 6618 (blue), and the five candidate OB stars identified by associated diffuse 24 μm emission (orange).

star (like bubble N49 in Watson et al. 2008), but there is only a faint hint of a PDR in the GLIMPSE 8.0 μm images, and this structure is not detected in the HHT CO maps. We have fit SEDs to every Archive source located within the ring, and we find no candidate early-type star apart from those included in Figure 14 and Table 5. Star 17 is the closest O star to the center of the ring, but it is not central enough to explain the ring geometry. The origin of the ring is therefore puzzling. Recent structural models of the M17 H II region suggest that the blister has broken to the North (Pellegrini et al. 2007; Povich et al. 2007), and hence could vent energy into the interior of M17 EB. The ring structure may be material blown from the side of the M17 H II region by such venting. This raises the possibility that NGC 6618 contributes energy to M17 EB.

5.2. Constraints on the Expansion Timescale of M17 EB

M17 EB is a PDR around a faint, diffuse H II region. In the classical model for an expanding H II region (neglecting stellar winds), the timescale for expansion to a radius R is given by

$$t_{\rm phot}[{\rm Myr}] = (3.175 \times 10^{-14}) \times \frac{4R_S}{C_{II}} \left[\left(\frac{R}{R_S} \right)^{\frac{7}{4}} - 1 \right], \quad (3)$$

from Equation (12)–(20) of Spitzer (1978). We assume typical properties of ionized gas at $T_e = 8000$ K: Isothermal sound speed $C_{\rm II} = 10$ km s^{-1} and recombination coefficient $\alpha^{(2)} = 3.09 \times 10^{-13}$ cm^3 s^{-1}. The Strömgren radius R_S depends upon the ambient ISM gas density n_0. We can make a rough estimate of n_0 from the column density of molecular gas swept up by the expansion of the bubble. Using the column density of molecular and atomic gas at $v = 12$–26 km s^{-1} derived from the CO emission (see Section 4.1), the total gas mass in M17 EB (including M17 North and part of MC G15.9−0.7) is $\sim$50, 000 $M_\odot$. If we model M17 EB as a thin spherical shell with diameter $2R = 20$ pc, then redistributing the gas throughout the shell interior yields a mean ambient density of $n_0 \sim 350$ cm^{-3}, consistent with an inhomogeneous molecular cloud environment. Photoionzed expansion driven by stars 17 and 18 in NGC 6618PG cannot produce an H II region the size of M17 EB within the stellar lifetimes ($t_{\rm phot} > 5$ Myr).

The expansion of M17 EB could instead be dominated by stellar winds. According to the analytical model of Weaver et al. (1977), the timescale for expansion of a windblown bubble to radius R is

$$t_{\rm wind}[{\rm Myr}] = \left[n_0 \left(\frac{R({\rm pc})}{27} \right)^5 \left(\frac{L_{\rm wind}}{10^{36}} \right)^{-1} \right]^{\frac{1}{3}}. \quad (4)$$

Typical wind luminosities for massive stars are $L_{\rm wind}/L_{\rm bol} = 2.5 \times 10^{-3}$ for dwarfs and $L_{\rm wind}/L_{\rm bol} \sim 5 \times 10^{-3}$ for giants (Vink et al. 2001). For a given n_0, wind-driven expansion produces a large bubble much more quickly than photoionized expansion. The Weaver et al. (1977) model with $n_0 \sim 350$ cm^{-3} and the same two driving stars produces M17 EB in $t_{\rm wind} < 1$ Myr.

The analytical models for both photoionized expansion and wind-driven expansion are oversimplifications of the physics governing the structure of H II regions. Both models underestimate the expansion timescales because they neglect radiative cooling by dust and, in the case of expansion driven by gas pressure (Equation (3)), depressurization caused by breaks in the bubble. Given the above caveats, the ideal case of photoionized expansion gives a lower limit on $t_{\rm phot}$ that exceeds the stellar lifetimes. In the wind-driven case, unless radiative cooling increases $t_{\rm wind}$ by a factor >10, expansion driven by wind momentum (Equation (4)) from the 2 most luminous stars in NGC 6618 PG can produce the bubble in $t_{\rm wind} < 5$ Myr. In the other limiting case of $t_{\rm wind} > 2$ Myr (see Section 5.1 above), the average expansion velocity of the bubble is 4.5 km s^{-1}, and the current velocity is lower because the expansion slows with time. The signature of such slow expansion would be undetectable in our spatially integrated CO line profiles (Section 4).

5.3. Sequence of Events

We now reconstruct a plausible star formation history for M17 based upon the wealth of observational data presented in this work.

Initially, the area shown within the white boundaries in Figure 15 was spanned by a large GMC complex that included the gas now observed in the M17 molecular cloud and MC G15.9−0.7. Between 2 and 5 Myr ago, a massive cloud subcomponent in the center of the complex underwent gravitational collapse, forming the first cluster of perhaps 2000–3000 stars, NGC 6618PG, the predecessor and possible progenitor of subsequent star formation in the complex. The OB stars in NGC 6618PG (blue diamonds in Figure 15) ionized an H II region that expanded, sweeping ambient ISM gas and dust into a bubble, M17 EB.

The M17 molecular cloud, with initial mass $>7 \times 10^4$ $M_\odot$, lay to the south of NGC 6618PG, in the path of the expanding M17 EB. What happened next is debatable. The onset of star formation in M17 may have been triggered when M17 EB collided with the M17 molecular cloud. But triggered star formation is impossible to prove, because we cannot prove that the molecular cloud would *not* have collapsed on its own, independent of the existence of NGC 6618PG. Indeed, it is curious that NGC 6618, the more massive cluster, formed later than NGC 6618PG. Measurements of the magnetic field strength in the PDR interface between the H II region and M17 South (see Figure 13) indicate that M17 South is in approximate dynamic equilibrium, with thermal, turbulent, and magnetic pressure combined supporting the cloud (Brogan & Troland 2001; Pellegrini et al. 2007). These support mechanisms might have allowed M17 initially to resist gravitational collapse.

The M17 molecular cloud began to collapse and form stars not more than 2 Myr ago. We know that NGC 6618 is younger than NGC 6618PG, because: (1) Despite being a more luminous cluster exhibiting many signs of strong stellar winds (Townsley et al. 2003; Povich et al. 2007, 2008), NGC 6618, unlike NGC 6618PG, has not yet dispersed its natal cloud; and (2) NGC 6618 has numerous highly embedded intermediate- to high-mass stars (ongoing massive star formation), while NGC 6618PG has no intermediate-mass stars with optically thick disks (massive star formation has ceased). The burst of star formation that created the most massive members of NGC 6618 was probably very rapid. The time-averaged SFR in the central regions of M17 has been 0.008–0.01 $M_\odot$yr^{-1}.

The presence of NGC 6618PG explains some puzzling features of the classic "blister" structure of the M17 H II region. Why should a blister H II region form in the first place?This question has received its share of theoretical attention in recent years. Two-dimensional models of molecular clouds with uniform density show that gravitational acceleration peaks at the edges of clouds, sweeping material inward (Burkert & Hartmann 2004). Heitsch et al. (2008) present three-dimensional numerical simulations that lead to the formation of massive

protostellar cores on the edges of molecular clouds facilitated by gravitational instabilities that focus large-scale colliding flows. M17 could be a good example of the end-product of such a process, with its cluster of very massive young stars forming on the northern side of the massive M17 South cloud. The CO maps show a narrow molecular ridge tracing M17 North that appears to be pressure-bounded on two sides. The ridge lies between NGC 6618 and NGC 6618PG (contours between NGC 6618 and NGC 6618PG in Figure 15). The source of outward pressure from the stars ionizing the M17 H II region is well-known, and we have now identified a potential source of counteracting pressure from the expansion of M17 EB. This provides a natural explanation for the morphology of the M17 North cloud and the associated northern half of the M17 H II region and PDR.

As the M17 H II region pushes outward from M17 South, M17 North is eroded. Once this barrier is breached, the built-up pressure in the H II region can be released into the diffuse interior of M17 EB. There are observational clues that this may already have occurred. The diffuse X-ray emission identified by Townsley et al. (2003) traces hot plasma filling the interior cavity of the M17 H II region. This plasma appears to spill out of the H II region to the east and north (L. K. Townsley et al. 2010, in preparation). The thermal radio/IR ring shown in Figure 14 may also be evidence of a blowout from the northern side of the H II region. In this scenario, it is possible that NGC 6618 now pumps energy into M17 EB, even though the bubble was originally driven by NGC 6618PG. Additional observations in X-rays and optical recombination lines are needed to reveal the detailed structure of M17 EB.

The expansion of M17 EB is asymmetric, with NGC 6618PG offset from the center of the bubble toward its southern rim, near M17 itself. This is reasonable given that the presence of the large molecular mass in M17 indicates a strong density gradient across the bubble. Any energy input from NGC 6618 into M17 EB would provide an additional push to expand the bubble preferentially away from the M17 H II region.

The northward expansion of M17 EB overtook another molecular cloud, MC 15.9−0.7. The central regions of MC G15.9−0.7 lack IR signatures of star formation. As Figure 15 shows, only the side of this cloud that intersects the 8 μm emission from M17 EB exhibits a significant concentration of candidate YSOs after the removal of background contaminants. Hence the circumstantial evidence for triggered star formation is stronger here than in the case of NGC 6618. Outside of M17 itself, the bubble-cloud interface produces the brightest CO ($J = 2 \rightarrow 1$) emission at $v = 20$ km s^{-1}. The current SFR in the molecular gas swept up by M17 EB and in the extended outer regions of M17 is >16% of the SFR that produced the well-studied young stellar population of the M17 H II region.

6. CONCLUSIONS

We have used IR, radio, and X-ray survey data combined with targeted millimeter observations to show that star formation in the M17 complex extends ∼0.°5 farther to the north than previously thought. Our ^{12}CO and ^{13}CO line maps cover a 0.72 deg^2 area that contains 1.35×10^5 $M_\odot$ in gas at $v = 12$–26 km s^{-1}. The morphology of the CO map (Figure 15) is dominated by an extended bubble, M17 EB, occupying the space between the well-studied M17 molecular cloud and a neighboring molecular cloud to the north, MC G15.9−0.7.

We have found 406 candidate YSOs in a $1.°5 \times 1°$ target field centered on M17 EB by fitting model SEDs to fluxes of sources in the GLIMPSE Archive supplemented by MIPSGAL and MSX photometry. We characterized the contamination from unassociated sources in our YSO sample by analyzing a control field exhibiting no obvious signs of massive star formation. We were able to identify and remove the brightest $\gtrsim$50% of dust-rich AGB stars from our sample. We conclude that >80% of sources in the control field sample are candidate YSOs distributed at unknown distances along the long sightline through the inner Galactic plane.

We created a map of the extinction produced by the molecular cloud structures associated with M17. Outside of a few small regions of high gas column density, across ∼90% of our target field the extinction is too low to significantly reduce mid-IR detections of background sources. The complex, spatially varying extinction in the M17 molecular cloud itself creates special challenges for observations of the young stellar population associated with NGC 6618. The average extinction through the cloud cavity occupied by the central M17 H II region is $A_V < 17$ mag, too low to prevent the detection of a significant fraction of background stars even for relatively shallow near-IR observations. Recent results reported by H08, in particular the high IR excess fraction and young age of 0.5 Myr for the young stellar population in M17, appear to have been compromised by the use of an IR-selected sample that was not corrected for background contamination.

Approximately half of the candidate YSOs in our target field are unassociated contaminants. In studies of massive young clusters, IR excess sources are commonly assumed to be associated by virtue of their apparent youth, but this assumption is not valid in the case of star-formation regions near the inner Galactic mid-plane. By selecting candidate YSOs exhibiting a significant degree of clustering with respect to the control sample, we successfully removed the predicted level of contamination.

Among 195 candidate YSOs overlapping the area occupied by the extended M17 complex, 96 have high statistical likelihood of association with M17 once the contribution from unassociated foreground and background sources is removed. Modeling the YSO population, we find that our sample consists primarily of intermediate-mass YSOs with disks (Stage II; Robitaille et al. 2006) and highly embedded (Stage 0/I) YSOs. We model the accretion rates for the Stage 0/I sources and find that their median age is $\lesssim$0.075 Myr, leading us to derive a circumstellar disk lifetime of ∼0.5 Myr for sources with $M_\star \gtrsim 3$ $M_\odot$ (corresponding to B-type stars on the main sequence). Candidate YSOs distributed around the rim of M17 EB and the extended outer regions of M17 represent a >16% addition to the SFR that has produced the young stellar population in the central regions of M17, as observed by *Chandra* (BFT07). The concentration of star formation activity tracing the interface between M17 EB and MC G15.9−0.7 appears to have been triggered by the expansion of the bubble.

We have identified five candidate ionizing stars inside M17 EB. By fitting stellar atmosphere models to their IR SEDs we constrained the luminosity distance of these five sources, showing that their IR luminosities give OB spectral types at the M17 distance. An associated lower-mass population of young stars is suggested by X-ray survey observations by the *Einstein* and *ROSAT* satellites, leading us to deduce the presence of a young cluster, NGC 6618PG. The two earliest-type stars in NGC 6618PG, BD-16 4831 and BD-16 4826 (stars 17 and 18 in Table 5), have luminosities equivalent to main-sequence spectral types O4–O5, but the stars may be evolved. The stellar

winds from these two stars carry sufficient momentum to produce an H II region the size of M17 EB in <5 Myr. The current expansion velocity of M17 EB is low, a few km s^{-1} maximum.

We also fit stellar atmosphere SEDs to 11 of the principal ionizing stars in NGC 6618. At the newly revised 2.1 kpc distance (H08), we find that a high fraction of the O stars in NGC 6618 are too luminous in the mid-IR to be single stars on the main sequence, yet the stars are too young to have evolved off the main sequence. This finding supports the hypothesis of H08 that most of the O stars in M17 are in binary systems with approximately equal-mass components.

The wealth of observational data paints a picture of propagating star formation in this region. Three main waves of star formation can be identified: (1) the formation of the NGC 6618PG cluster (2000–3000 stars), 2–5 Myr in the past, followed by the expansion of an H II region delineated by M17 EB; (2) the rapid collapse of the M17 molecular cloud (current mass $>6 \times 10^4$ $M_\odot$) within the last 2 Myr, producing the massive NGC 6618 cluster and associated massive star formation that continues to the present day (11,000–14,000 stars); (3) the onset of star formation in MC G15.9−0.7 and the extended outer regions of M17 (>1000 stars). The possibility that the later waves of star formation were triggered by the first raises a tantalizing question: Can a massive progenitor cluster trigger the formation of an even more massive daughter cluster?

Because they are beacons observable at large distances across the local universe, H II regions are commonly used as SFR tracers in external galaxies, and have been used to estimate the SFR of the Milky Way as well (Smith et al. 1978). The canonical Galactic SFR of a few $M_\odot yr^{-1}$ is equivalent to several hundred H II regions the size of M17. Observational tracers tied to H II regions are sensitive only to the most massive <1% of stars, and the uncertainty involved in extrapolating over the IMF to the low-mass stars that make up the bulk of the stellar mass is enormous. Star formation distributed at lower densities but over large spatial volumes is increasingly observed in prominent Galactic molecular cloud complexes, including Orion (Megeath et al. 2005), W5 (Koenig et al. 2008), and now M17. It is not yet clear if low-density star formation outside of bright H II regions or dense GMCs significantly increases the galactic SFRs derived from observational tracers of ionized or molecular gas.

We are indebted to Leisa Townsley for keen insights and suggestions that helped guide this work and for sharing early results from *Chandra*. We thank the anonymous referee for numerous comments that helped to substantially improve this work. Frank D. Ghigo, Ronald J. Maddalena, and Dana S. Balser provided the GBT 3 cm image used in our analysis. We thank Steve Bracker for IR color analysis of candidate AGB stars, David Pooley for finding the *Einstein* image, and Cormac Purcell for inspecting the CORNISH survey images on our behalf. Conversations with Debra Shepherd, Fabian Heitsch, and Kyle Westfall helped improve this work. We thank Dr. A. R. Kerr of the National Radio Astronomy Observatory for providing the single-sideband ALMA Band 6 prototype mixers used in this study. The Heinrich Hertz Telescope is operated by the Arizona Radio Observatory, a part of Steward Observatory at The University of Arizona. This work was supported by NASA/JPL contract 1275394 and NSF grant AST-0303689 to the University of Wisconsin. Additional support was provided by the *Spitzer* Theoretical Research Program (1290701 & 1310231; B.A.W., T.P.R.), the NASA Theory Program (NNG05GH35G; B.A.W.), and NSF grant AST-0708131 to The University of Arizona (M.K., J.H.B.). M.K. gratefully acknowledges support from a Korea Research Foundation Grant (KRF-2007-612-C00050). Additional support was provided by NASA through the *Spitzer Space Telecopse* Fellowship Program (T.P.R.). This work relies on observations made using the *Spitzer Space Telescope*, operated by the Jet Propulsion Laboratory under a contract with NASA. This research has made use of the SIMBAD database, operated at CDS, Strasbourg, France. This work has also made use of data obtained from the High Energy Astrophysics Science Archive Research Center (HEASARC), provided by NASA's Goddard Space Flight Center.

Facilities: Spitzer, HHT, MSX, GBT, VLA

REFERENCES

Allen, L., et al. 2004, ApJS, 154, 363, A04
Benjamin, R. A., et al. 2003, PASP, 115, 953
Bernasconi, P. A., & Maeder, A. 1996, A&A, 307, 829
Bohlin, R. C., Savage, B. D., & Drake, J. F. 1978, ApJ, 224, 132
Bressan, A., Fagotto, F., Bertelli, G., & Chiosi, C. 1993, A&AS, 100, 647
Brogan, C. L., Gelfand, J. D., Gaensler, B. M., Kassim, N. E., & Lazio, T. J. W. 2006, ApJ, 639, L25
Brogan, C. L., & Troland, T. H. 2001, ApJ, 560, 821
Broos, P. S., et al. 2007, ApJS, 169, 353, BFT07
Brott, I., & Hauschildt, P. H. 2005, in The Three-dimensional Universe with *Gaia*, ed. C. Turon, K. S. O'Flaherty, & M. A. C. Perryman (ESA SP-576; Noordwijk: ESA), 565
Burkert, A., & Hartmann, L. 2004, ApJ, 616, 288
Carey, S. J., et al. 2009, PASP, 121, 76
Carigi, L., & Peimbert, M. 2008, RevMexAA, 44, 341
Cesarsky, C. J., Cesarsky, D. A., Lequeux, J., & Churchwell, E. 1978, A&A, 68, 33
Cesarsky, D., Lequeux, J., Abergel, A., Perault, M., Palazzi, E., Madden, S., & Tran, D. 1996, A&A, 315L, 309
Chini, R., Elsässer, H., & Neckel, T. 1980, A&A, 91, 186, CEN
Chini, R., Hoffmeister, V. H., Kämpgen, K., Kimeswenger, S., Nielbock, M., & Siebenmorgen, R. 2004a, A&A, 427, 849
Chini, R., Hoffmeister, V., Kimeswenger, S, Nielbock, M., Nürnberger, D., Schmidtobreick, L, & Sterzik, M. 2004b, Nature, 429, 155
Chini, R., & Wargau, W. F. 1998, A&A, 329, 161
Churchwell, E., et al. 2006, ApJ, 649, 759
Cohen, M. 1993, AJ, 105, 1860
Cox, A. N., ed. 2000, Allen's Astrophysical Quantities (4th ed.; Berlin: Springer)
Cyganowski, C. J., et al. 2008, AJ, 136, 2391
Davis, C. J., Kumar, M. S. N., Sandell, G., Froebrich, D., Smith, M. D., & Currie, M. J. 2007, MNRAS, 374, 29
Dunne, B. C., Chu, Y.-H., Chen, C.-H. R., Lowry, J. D., Townsley, L., Gruendl, R. A., Guerrero, M. A., & Rosado, M. 2003, ApJ, 590, 306
Elmegreen, B. G., & Lada, C. J. 1976, AJ, 81, 12
Fazio, G. G., et al. 2004, ApJS, 154, 10
Felli, M., Churchwell, E., & Massi, M. 1984, A&A, 136, 53, FCM84
Felli, M., Testi, L., Schuller, F., & Omont, A. 2002, A&A, 392, 971
Guandalini, R., Busso, M., Ciprini, S., Silvestro, G., & Persi, P. 2006, A&A, 445, 1069
Gutermuth, R. A., et al. 2008, ApJ, 674, 336, G08
Haisch, K. E., Lada, E. A., & Lada, C. J. 2000, AJ, 120, 1396
Haisch, K. E., Lada, E. A., & Lada, C. J. 2001a, AJ, 121, 2065
Haisch, K. E., Lada, E. A., & Lada, C. J. 2001b, ApJ, 553, L153
Handa, T., Sofue, Y., Nakai, N., Hirabayashi, H., & Inoue, M. 1987, PASJ, 39, 709
Hanson, M. M., Howarth, I. D., & Conti, P. S. 1997, ApJ, 489, 698
Heitsch, F., Hartmann, L. W., Slyz, A. D., Devriendt, J. E. G., & Burkert, A. 2008, ApJ, 674, 316
Hoffmeister, V. H., Chini, R., Scheyda, C. M., Schulze, D., Watermann, R., Nürnberger, D., Vogt, N., & Nielbock, M. 2008, ApJ, 686, 310, H08
Høg, E., et al. 2000, A&A, 355, 27L
Hony, S., Waters, L. B. F. M., & Tielens, A. G. G. M. 2002, A&A, 390, 533
Indebetouw, R., Robitaille, T. P., Whitney, B. A., Churchwell, E., Babler, B., Meade, M., Watson, C., & Wolfire, M. 2007, ApJ, 666, 321
Indebetouw, R., et al. 2005, ApJ, 619, 931
Jaffe, D. T., & Fazio, G. G. 1982, ApJ, 257, L77
Jiang, Z., et al. 2002, ApJ, 577, 245, J02
Kenyon, S. J., & Hartmann, L. 1995, ApJS, 101, 117

Kleinmann, D. E., & Wright, E. L. 1973, ApJ, 185, L131
Koenig, X. P., Allen, L. E., Gutermuth, R. A., Hora, J. L., Brunt, C. M., & Muzerolle, J. 2008, ApJ, 688, 1142
Kulesa, C. A., Hungerford, A. L., Walker, C. K., Zhang, X., & Lane, A. P. 2005, ApJ, 625, 194
Kurucz, R. 1993, ATLAS9 Stellar Atmosphere Programs and 2 km s^{-1} grid. Kurucz CD-ROM No. 13. (Cambridge, MA: Smithsonian Astrophysical Observatory)
Kutner, M. L., & Ulich, B. L. 1981, ApJ, 250, 341
Lada, C. 1976, ApJS, 32, 603
Lada, C. J. 1987, in IAU Symp. 115, Star Forming Regions, ed. M. Peimbert, J. Jugaku (Dordrecht: Kluwer), 1
Lada, C. J., DePoy, D. L., Merrill, K. M., & Gatley, I. 1991, ApJ, 374, 533
Martins, F., Schaerer, D., & Hillier, D. J. 2005, A&A, 436, 1049
Mason, B. D., Hartkopf, W. I., Greis, D. R., Henry, T. I., & Helsel, J. G. 2009, AJ, 137, 3358
McClure-Griffiths, N. M., Dickey, J. M., Gaensler, B. M., Green, A. J., Haverkorn, M., & Strasser, S. 2005, ApJS, 158, 178
Megeath, S. T., et al. 2005, in IAU Symp. 227, Massive Star Birth: A Crossroads of Astrophysics, ed. R. Cesaroni, M. Felli, E. Churchwell, & C. M. Walmsley (Dordrecht: Kluwer), 383
Mizuno, A., & Fukui, Y. 2004, in ASP Conf. Ser. 317, Milky Way Surveys: The Structure and Evolution of Our Galaxy, ed. D. Clemens, R. Y. Shah, & T. Brainerd (San Francisco, CA: ASP), 59
Muench, A. A., Lada, E. A., Lada, C. J., & Alves, J. 2002, ApJ, 573, 366
Nielbock, M., Chini, R., Jütte, M., & Manthey, E. 2001, A&A, 273, 284
Ogura, K., & Ishida, K. 1976, PASJ, 28, 35, OI
Pellegrini, E. W., et al. 2007, ApJ, 658, 1119
Porras, A., et al. 2007, ApJ, 656, 493
Povich, M. S., Benjamin, R. A., Babler, B. L., Indebetouw, R., Meade, M. R., Whitney, B. A., & Churchwell, E. 2008, ApJ, 689, 242
Povich, M. S., et al. 2007, ApJ, 660, 346, PSC07
Preibisch, T., et al. 2005, ApJS, 160, 401
Price, S. D., Egan, M. P., Carey, S. J., Mizuno, D. R., & Kuchar, T. A. 2001, AJ, 121, 2842
Purcell, C. R., Hoare, M. G., & Diamond, P. 2008, in ASP Conf. Ser. 387, Massive Star Formation: Observations Confront Theory, ed. H. Beuther, H. Linz, & T. Henning (San Francisco, CA: ASP), 389
Reich, W., Fuerst, E., Reich, P., & Reif, K. 1990, A&AS, 85, 633
Richer, J. S., Shepherd, D. S., Cabrit, S., Bachiller, R., & Churchwell, E. 2000, in Protostars and Planets 4, ed. V. Mannings, A. Boss, & S. Russell (Tucson, AZ: Univ. of Arizona Press), 867
Robitaille, T. P., Whitney, B. A., Indebetouw, R., & Wood, K. 2007, ApJS, 169, 328, RW07
Robitaille, T. P., Whitney, B. A., Indebetouw, R., Wood, K., & Denzmore, P. 2006, ApJS, 167, 256, RW06
Robitaille, T. P., et al. 2008, AJ, 136, 2413
Sanders, D. B., Clemens, D. P., Scoville, N. Z., & Solomon, P. M. 1986, ApJS, 60, 1
Salpeter, E. E. 1955, ApJ, 121, 161
Sana, H., Gosset, E., Nazé, Y., Rauw, G., & Linder, N. 2008, MNRAS, 386, 447
Sault, R. J., Teuben, P. J., & Wright, M. C. H. 1995, in ASP Conf. Ser. 77, Astronomical Data Analysis Software and Systems IV, ed. R. Shaw, H. E. Payne, & J. J. E. Hayes (San Francisco, CA: ASP), 433
Sewilo, M., Churchwell, E., Kurtz, S., Goss, W. M., & Hofner, P. 2004, ApJ, 605, 285
Shepherd, D. S., et al. 2007, ApJ, 669, 464
Siess, L., Dufour, E., & Forestini, M. 2000, A&A, 358, 593
Skrutskie, M. F., et al. 2006, AJ, 131, 1163
Smith, L. F., Biermann, P., & Mezger, P. G. 1978, A&A, 66, 65
Smith, H. A., Hora, J. L., Marengo, M., & Pipher, J. L. 2006, ApJ, 645, 1264
Spitzer, L. 1978, Physical Processes in the Interstellar Medium (New York: Wiley)
Stetson, P. 1987, PASP, 99, 191
Sylvester, R. J., Kemper, F., Barlow, M. J., de Jong, T., Waters, L. B. F. M., Tielens, A. G. G. M., & Omont, A. 1999, A&A, 352, 587
Townsley, L. K., Feigelson, E. D., Montmerle, T., Broos, P. S., Chu, Y.-H., & Garmire, G. P. 2003, ApJ, 593, 874
van Dishoeck, E., & Black, J. H. 1988, ApJ, 334, 771
Verstraete, L., Puget, J. L., Falgarone, E., Drapatz, S., Wright, C. M., & Timmermann, R. 1996, A&A, 315L, 337
Vink, J. S., de Koter, A., & Lamers, H. J. G. L. M. 2001, A&A, 369, 574
Wainscoat, R. J., Cohen, M., Volk, K., Walker, H. J., & Schwartz, D. E. 1992, ApJS, 83, 111
Wallerstein, G., & Knapp, G. R. 1998, ARA&A, 36, 369
Watson, C., et al. 2008, ApJ, 681, 1341
Weaver, R., McCray, R., Castor, J., Shapiro, P., & Moore, R. 1977, ApJ, 218, 377
Weingartner, J. C., & Draine, B. T. 2001, ApJ, 548, 296
Whitney, B. A., Indebetouw, R., Bjorkman, J. E., & Wood, K. 2004, ApJ, 617, 1177
Whitney, B. A., Wood, K., Bjorkman, J. E., & Wolff, M. J. 2003a, ApJ, 591, 1049
Whitney, B. A., Wood, K., Bjorkman, J. E., & Cohen, M. 2003b, ApJ, 598, 1079
Whitney, B. A., et al. 2008, AJ, 136, 18
Wilson, C. D., Howe, J. E., & Balogh, M. L. 1999, ApJ, 517, 174
Wood, D. O. S., & Churchwell, E. 1989, ApJ, 340, 265